Smartphone-enabled Biotelemetric System For a Smart Contact Lens

by

Luyao Chen

A thesis
presented to the University of Waterloo
in fulfillment of the
thesis requirement for the degree of
Master of Applied Science
in
Electrical and Computer Engineering

Waterloo, Ontario, Canada, 2017

I hereby declare that I am the sole author of this thesis. This is a true copy of the thesis, including any required final revisions, as accepted by my examiners.

I understand that my thesis may be made electronically available to the public.

Abstract

Diabetes describes a disordered metabolic state with an overabundance of glucose in the bloodstream, due to insufficient production or utilization of insulin to allow tissue cells from consuming glucose. People with unmanaged diabetes could lead to many serious complications such as heart disease, stroke, coma, kidney failure, blindness, amputation, and premature death. Diabetes can be managed by monitoring the blood glucose level, and control the glucose level by taking insulin, and exercising a carefully planned lifestyle with appropriate diet and physical activities. An elegant solution for glucose monitoring is the integration of electrochemical-based glucose sensor and microelectronics within a contact lens, namely a smart contact lens, which can measure the tear glucose in the eye, and correlate it to blood glucose. Currently, there is no functional smart contact lens devices for glucose detection in the market.

This thesis focuses on providing proof of concept prototypes for implementing energy harvesting and wireless data transmission on a smart contact lens. An all-in-one solution is proposed to harvest energy from a smartphone, and use the same smartphone to support glucose data extraction by backscattering. The appropriate prototype architectures are justified based on a system specification estimated from related works. The prototypes are designed in simulation, and then fabricated on PCBs using off-the-shelf components and equipment. Measurements are conducted on the prototypes to evaluate their performance against the initial assessment of requirements from related works.

Acknowledgements

I would like to thank Dr. Safieddin Safavi-Naeini and Dr. George Shaker for providing support and supervision to this research; special thanks to Medella Health Inc. for making the results of this research relevant to the high-tech industry.

Table of Contents

List of Tables

List of Figures

Chapter 1

Introduction: the Importance of Glucose Monitoring in Diabetes Management

Diabetes mellitus, or more commonly known as just diabetes, is a disease directly caused by failure of the pancreas in both human and animals. The function of the pancreas is to produce a steady supply of hormone insulin, because insulin enables the body's cells to accept glucose (simple sugar) in the bloodstream as caloric energy. Diabetes describes a disordered metabolic state with an overabundant of glucose in the bloodstream, due to insufficient production or utilization of insulin to allow the cells from consuming glucose. People with unmanaged diabetes could lead to many serious complications such as heart disease, stroke, coma, kidney failure, blindness, amputation, and premature death [1].

Diabetes is classified into two categories: type 1 and type 2. As of 2014, 9.3% of the U.S. and Canadian population have diabetes. In adults, type 1 diabetes accounts for approximately 5% of all diagnosed cases, with the rest being type 2 diabetes [1][2]. Type 1 describes diabetic patients without the capability to produce hormone insulin from the destruction of beta cells in the pancreas, which could happen at any age. Type 1 patients must inject insulin artificially from an external source. There is currently no known way to prevent type 1 diabetes. Type 2 describes diabetic patients with insulin-resistant cells that underutilizes existing insulin produced by the pancreas, which creates an insulin deficiency throughout the body. Type 2 patients are able to manage diabetes by monitoring their glucose level, and control the glucose level by exercising a carefully planned lifestyle with appropriate diet and physical activities [3].

The Canadian Diabetes Association recommends monitoring of blood glucose at least as often as insulin intake (four times daily) for type 1 patients, and two times daily for type 2 patients to meet glycemic targets [4]. To check for blood glucose, blood from the tip of the finger is drawn, and then analyzed on a glucometer. Finger-pricking has been the only medically accepted glucose monitoring technique for diabetic patients until as recent as 2012, when the US Food and Drug Administration has approved its first continuous glucose monitoring (CGM) system, which uses the so called artificial pancreas as an automated closed-loop glucose detection and insulin administration device that lessens the frequency of daily finger-pricking [5]. However, artificial pancreas also performs glucose analysis invasively through the skin, which is non-ideal or non-feasible in many health monitoring applications.

1.1 Existing Technologies in Glucose Monitoring

From the perspective of device operation, the methods of glucose monitoring can be essentially categorized as invasive, minimally-invasive, and non-invasive [6]. Invasive devices detect glucose from subcutaneous or intravenous bodily fluids: besides analyzing glucose level via blood drawn from the finger, there are wireless implants with radio frequency capabilities to communication glucose data to an external controller for analysis [7]. Minimally-invasive devices detect glucose externally via extracted interstitial fluid from skin tissues. They differ from invasive devices in that the techniques to extract interstitial fluid do not cause significant damage to the tissue. Some technologies include iontophoresis and sonophoresis, where interstitial fluid is extracted using electric current and ultrasound, respectively [8][9]. There is discomfort and risks of infection from both invasive and minimally-invasive techniques, and researchers in both academia and industry are working on non-invasive techniques for detecting glucose from external body-fluids such as sweat and tear [10][11][12].

Tear in the eye exists in different states: "Basal" tear is the nominal flow of fresh tear fluid secreted from the lacrimal glands located at the upper corner of each eye as shown in Figure 1.1; "Reflex" tear is caused by irritation of the eye; "Psychic" tear refers to tear from crying and emotional stress [14]. In all cases, tear acts as a liquid film interfacing the ocular surface and outside environment. Under Basal conditions, the tear flows across the eye at a reasonably stable volume in three distinct layers: a surface lipid layer (0.2um thick), a middle aqueous layer (8um thick), and an inner mucin layer (0.3um thick). Glucose in the aqueous layer has a predictable concentration of 0.1 to 0.6 mM under Basal state, and it has a well-established correlation to blood glucose [15]. Since

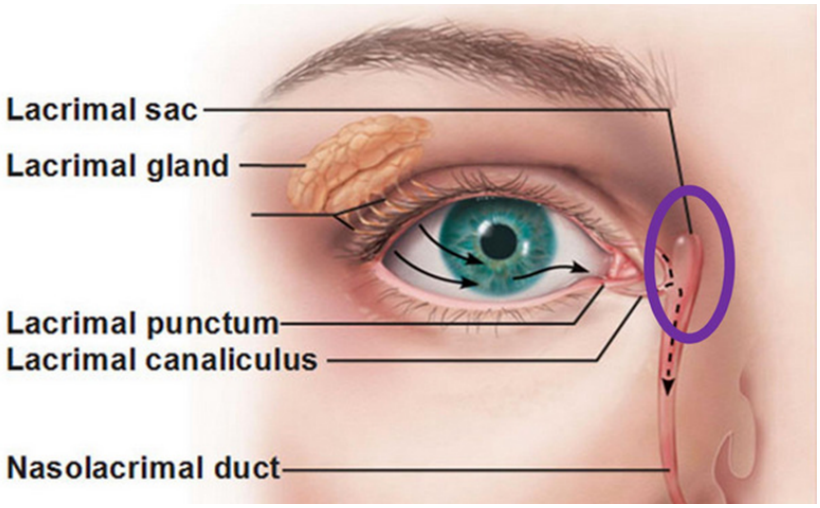

Figure 1.1: Direction of tear flow across the surface of a human eye [13].

the tear is always accessible externally, it is possible to analyze glucose level using ocular spectroscopy, where the glucose concentration in tear is directly indicated as a change of color to the fluorophore-based sensor [6]. Although this type of measurement is truly non-invasive, it is very difficult to quantify the color change to perform meaningful data analysis of glucose level. Moreover, optical detection technology is often single-use, which renders it infeasible for continuous glucose monitoring.

To improve the practicality of detecting tear glucose in real-world scenarios, electrochemical based methods for tear glucose sensing are developed similar to that for blood glucose. Generally, the electrochemical-based sensor catalyzes the oxidation of glucose, converting the glucose to a reduced form with free electrons as a byproduct, which forms an amperometric current that correlates to a specific glucose concentration [6].

Minimally, there must exist an electrochemical-based sensor submerged in the tear fluid, and a potentiostat circuit to sustain the amperometric reaction of the sensor with glucose found in the tear. The op-amp in Figure 1.2 regulates a constant voltage, controlled by a bias, between reference electrode and the glucose sensor (on the working electrode). At the same time, an amperometric current flows between the counter electrode and the sensor caused by its electrochemical reaction to glucose. In conjunction with known sensor characteristics, a measuring instrument such as an ammeter in the path of the current can be used to determine the glucose concentration in the tear fluid [16]. It is possible to extract two to three microliters of tear using a hollow capillary tube. This method of tear collection is well tolerated in clinical settings and does not cause any adverse effects to the

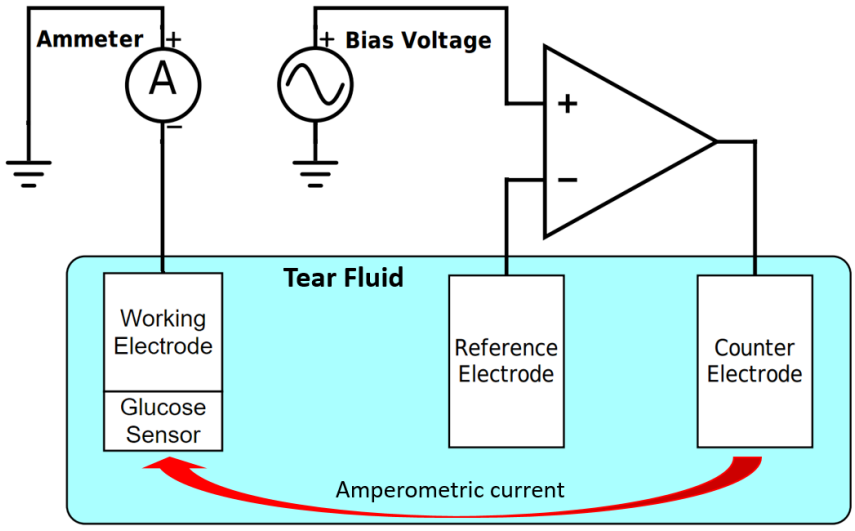

Figure 1.2: Measuring amperometric current via a simplified potentiostat, sensor, and ammeter.

eye. Similar to the way that blood glucose is analyzed via a glucometer, tear fluid from the capillary tube can be pushed out onto the sensor surface for single data point analysis. In practice, tear extraction via capillary tube often agitates the eye, and causes flow of Reflex tears, which can distort the accuracy of the tear glucose data when compared to the standard blood glucose.

An elegant solution is the integration of electrochemical-based glucose sensor and microelectronics with a contact lens, namely a smart contact lens. Figure 1.3 shows a smart contact lens developed by Alphabet Inc.'s life science research organization—Verily [18][19][20]. It features electrochemical glucose sensing and wireless radio capabilities, which are encapsulated between regular soft contact lens material. When the smart contact lens is worn, it floats in-between the aqueous layer and the inner mucin layer. This minimizes irritation of the cornea, and still gives the electrochemical sensor access to the glucose in the aqueous layer. In addition, the smart contact lens has a functional lifetime only limited by the durability of the electrochemical sensor, which could be up to a month if the sensor is non-enzymatic. Currently, there is no functional smart contact lens devices for glucose detection, but there are research papers detailing possible use-cases and suitable technologies for tackling some critical aspects on the development of the smart contact lens.

The contact lens dictates the final form of the device structure, including the sensor and microelectronics. Hard contact lenses, composed of pure silicone or fluorosiloxane acrylate,

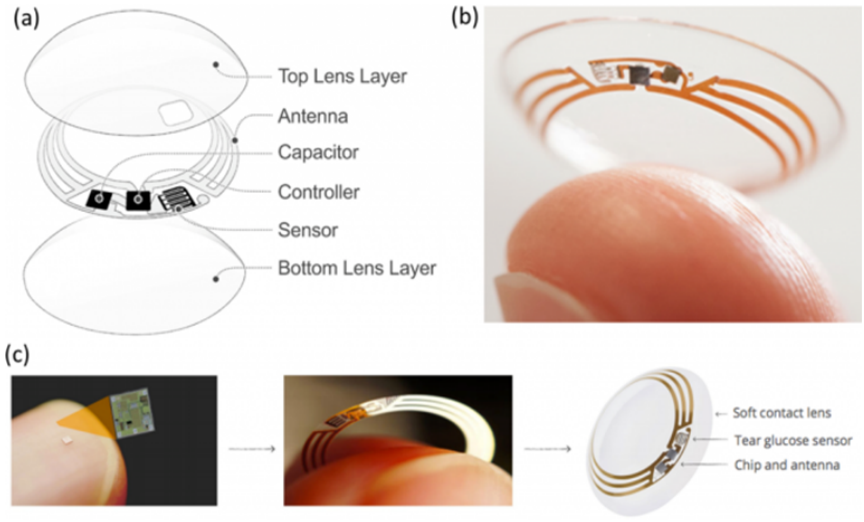

Figure 1.3: A prototype smart contact lens from Verily [17].

may cover the cornea with dimensions between 5.9mm to 7.8mm in diameter [21]. Soft contact lenses are composed of a mixture of highly water absorbent (hydrogel) hydrophilic polymers with much larger dimensions between 14mm to 15mm in diameter [22]. Thickness of soft and hard contact lens are non-uniform across the structure, but it is generally no more than 200um to ensure comfort for the wearer. Such limited space available on the contact lens give rise to the issue of providing power to support critical functions for the on-lens microelectronics. Sub-100uW biased potentiostat circuit has shown to be capable of generating amperometric signal from an electrochemical-based glucose sensor. Additional power also has to be considered for extracting glucose data from the contact lens to an external reader to perform analysis, which requires a wireless solution. Backscatter radio is shown to be a favored solution, because it has a low on-lens operating power requirement, and a small circuit footprint ideal for implementation on the contact lens [23].

The contact lens and the external reader can be described as an asymmetric system in terms of functionality. The restrictive dimension of the contact lens limits the on-lens hardware to a minimum, and transfers the functional complexity to the reader side. From the perspective of a smart contact lens user, the glucose data is captured, displayed, and stored on this reader. There is no need for the user to actively control the smart contact lens. The responsibility of the smart contact lens system is satisfied as long as glucose level can be tracked throughout the day, and the data can construct easily understandable glucose trends to simplify diabetes management.

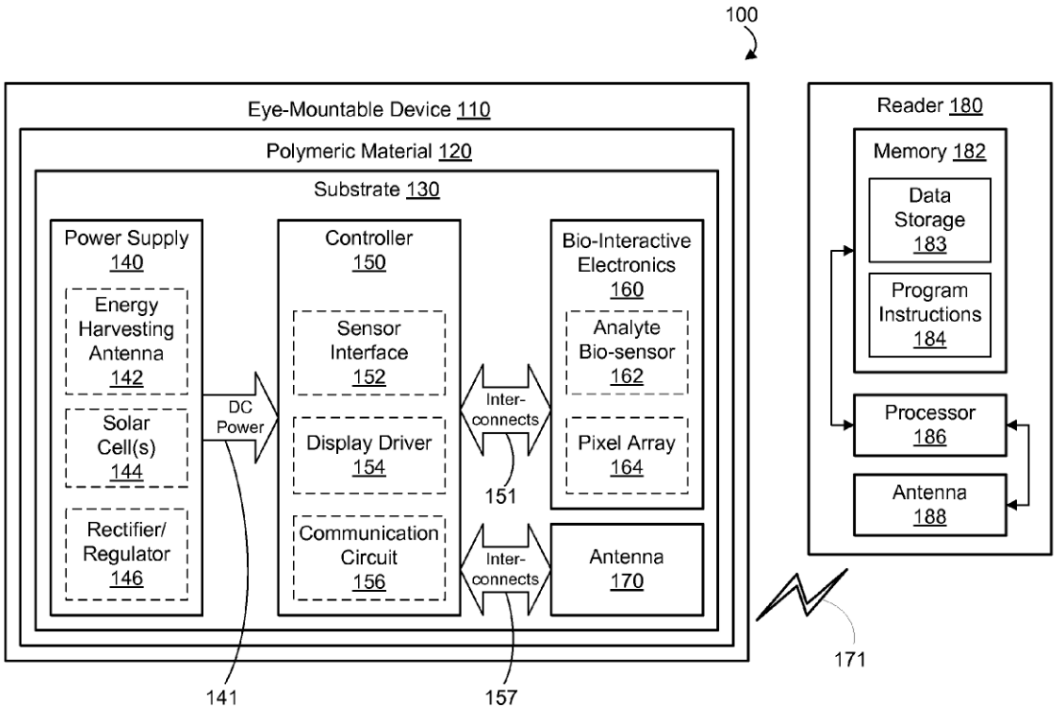

Figure 1.4: Methods and system for interfacing a smart contact lens from Verily [18].

Figure 1.4 shows Verily's patent claim of an example block diagram of an asymmetric eye-mountable device in wireless communication with an external reader. The eye-mountable device is euphemism for a smart contact lens, which supports bio-interactive electronics like a potentiostat, communication module for transferring the glucose level to the reader, and power supply circuits for energy harvesting and rectification to DC power. Besides the fundamental blocks, the patent claims include various embodiments on the implementation of each block. For example, it is left open whether communication would utilize traditional radio or backscattering, and whether wireless power transfer from the reader or sole on-lens energy harvesting would be used as the power source.

1.2 Contribution of Thesis

This thesis focuses on providing proof-of-concept for implementing energy harvesting and wireless data acquisition on a smart contact lens to the reader system. An all-in-one so-

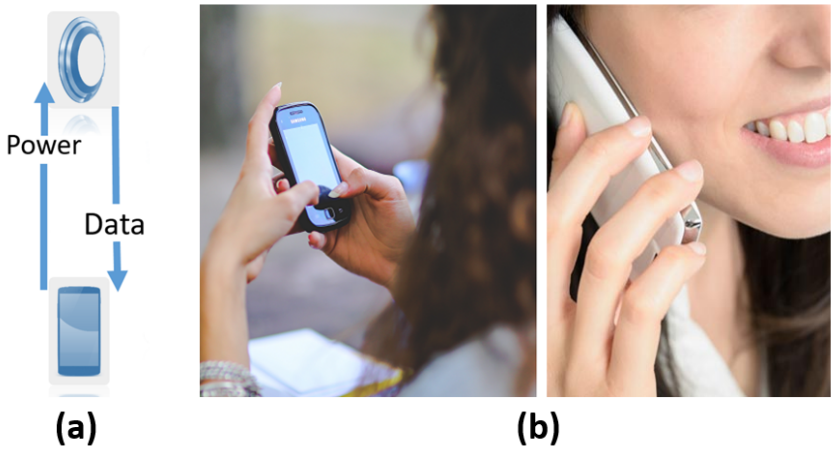

Figure 1.5: Intended use cases of the smart contact lens: a) role of the smartphone ; b) location of smartphone.

lution is proposed to harvest energy from a smartphone, and use the same smartphone to support glucose data extraction by backscattering as shown in Figure 1.5a. In scenarios similar to Figure 1.5b, where a person wearing the smart contact lens raises the smartphone to a close proximity to the lens, the smart contact lens rectifies cellular emission to DC power to sustain operations of the on-lens microelectronics; while powered, the smart contact lens modulates the glucose data in frequency to support direct wireless backscattering communication with the smartphone.

The goal of the proof-of-concept prototypes is twofold:

1. to quantify the amount of power that a smart contact lens can realistically harvest from cellular emission, which serves as a guideline for the upper and lower bounded limitation on power consumption for the on-lens microelectronics.

2. to demonstrate a viable implementation of a backscattering system that enable the transmission of glucose data directly from the smart contact lens to the smartphone.

1.3 Organization of Thesis

The reminder of this thesis is organized into three chapters. Chapter 2 discusses the relevant smartphone technologies to be considered for this proposed design, as well as a general

overview of the functionalities of the smart contact lens that would set the requirement for development of the proof of concept prototypes. Chapter 3 discusses using cellular emission of a smartphone as a RF energy source, and how energy harvesting on the smart contact lens can take advantage this RF source. Chapter 4 discusses the implementation of a backscatter module as the communication system on the smart contact lens. Chapter 3 and Chapter 4 include the design, fabrication, and measurement of the proof of concept prototypes. Chapter 5 discusses the conclusion found in this thesis.

Chapter 2

System Design Between a Smartphone and a Smart Contact Lens

An understanding of the general functionalities of the smart contact lens and the characteristics of a smartphone is essential in determining the design requirements of the proof of concept prototypes. In this chapter, the method of wireless glucose data backscattering communication is explained, and an overview of the critical components on the smart contact lens is given to define the estimated requirement on power budget.

2.1 Method of Lens-to-Phone Communication

Backscattering has been adapted extensively in RFID devices, and it is recently demonstrated to function with smartphones in a trending technology development called *infrastructureless* RFID, where the idea is to utilize existing radio-enabled personal devices to act as an interrogator to communicate with simple transponders over a much longer distance than the intended application of current NFC platforms. Continued rise in popularity of such premise in backscattering technology could lead to a wide adaption in future development of smartphones, where low-powered wearable devices like the smart contact lens could take advantage of the smartphone as a centralized platform for wireless telemetry.

Smartphones in the current market supports a wide array of cellular networks (e.g. GSM, CDMA, LTE), Wi-Fi, and Bluetooth. The need of an energy efficient wireless

personal area network on the smartphone platform has branched Bluetooth into multiple categories, with Bluetooth Low Energy (BLE) aimed at applications with low data rate and low power consumption. BLE has two modes of operation: peer to peer communication that requires handshake authentication between a pair of interchangeable transmitting and receiving devices, and broadcast communication where a transmitting device can broadcast data to an arbitrary number of non-connectable devices in proximity of the broadcaster. Usually, the broadcaster is a simple low-power tag, and smartphone the receiver. Since the BLE broadcast mode is implemented on its advertisement channels, the smartphone will always be listening to the broadcaster as long as Bluetooth is enabled on the device. This makes the smartphone a perfect receiver for backscattered signal, because there is no demand for inter-device authentication, and the smartphone is always ready to receive the backscattered signal.

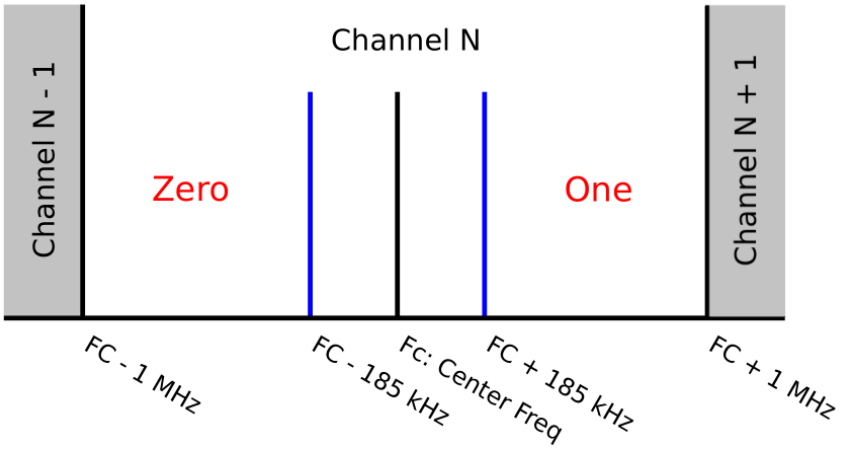

Figure 2.1: Channel layout of a single 2-MHz wide BLE channel [24].

Basic BLE utilizes a Gaussian-filtered BFSK modulation with a channel bandwidth of 2-MHz per channel. Figure 2.1 depicts the layout of a single BLE channel. For each BLE channel, the BLE carrier signal corresponds to the center frequency of that channel. A frequency deviation of 185-KHz above the center frequency corresponds to a binary bit 1; vice versa, a frequency deviation of 185-KHz below the center frequency corresponds to a binary bit 0. The BLE data rate is defined at 1-MHz, which means that each bit takes 1us to transmit. The detailed spectrum requirements are found on the Bluetooth Core Specification documentation.

In BLE broadcast mode, the signal is also emitted from the Bluetooth advertisement channels in the form of digital packet data. The BLE advertisement data packet frame is

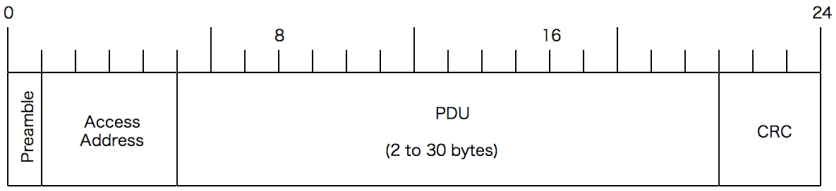

Figure 2.2: BLE packet frame format [25].

shown in Figure 2.2. Each frame can be between 80 bits to 376 bits in length, where the actual Payload Data Unit (PDU) is a variable dependent on the need of the data size, and the mandatory overhead allocated to define the following:

- Preamble—for detecting the beginning of a data frame
- Access Address—for identifying the purpose of the data frame, which is a constant value for identifying the advertisement frame (0x8E89BED6)
- Cyclic Redundancy Check (CRC)—for detecting possible corruption of data during transmission
- Payload Data Unit properties—2 reserved byte in the PDU for describing the purpose and characteristics of the payload

The PDU has a maximum size of 28 bytes reserved for transmitting glucose data from the smart contact lens.

Each symbol in the BFSK signal constellation used by Bluetooth may be represented by a set of complex coordinates defined by S on the IQ plane shown in Figure 2.3c. It follows that both the In-phase and Quadrature components of the complex coordinate $S_{1,2}$ are controllable by the complex impedance of the load $Z_{1,2}$, which can also be mapped to a corresponding reflection coefficient $\Gamma_{1,2}$ in Figure 2.3b, when referenced to a specific antenna impedance and operating frequency. Under a time-varying load between Z_1 and Z_2 shown in Figure 2.3a, the key observation is that the scattered electric field is influenced by the reflection coefficient both in its amplitude and phase to create a binary signal. More specifically, a set of points in the IQ plane is defined by a set of impedance that produces desired amplitude and phase change in the scattered electric field, which allows for communication of the smart contact lens and the smartphone via the BFSK constellation utilized by Bluetooth Low Energy.

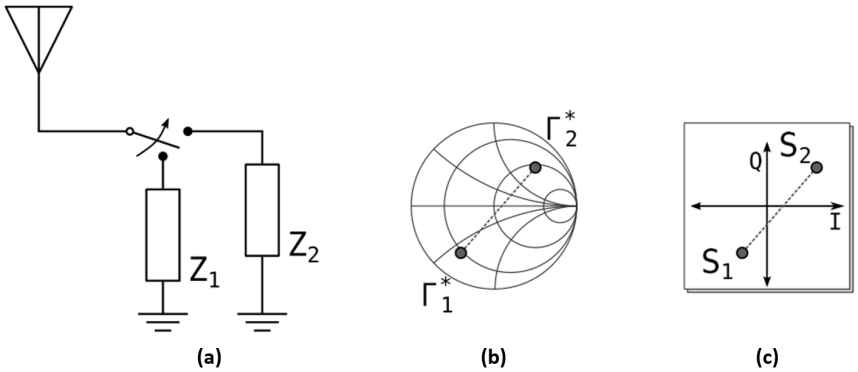

Figure 2.3: With reference to the reference antenna: a) load impedance, b) location on the Smith chart, c) signal on the IQ plane [26].

2.1.1 Construction of BLE Baseband

It is mentioned in Chapter 1 that glucose can be consumed through electrochemical redox by a potentiostat to produce an electrical current, which correlates to a specific glucose concentration in the tear fluid. Figure 2.4 shows the averaged amperometric response of three independent measurements of tear glucose from a sensor embedded in a soft hydrogel contact lens [27].

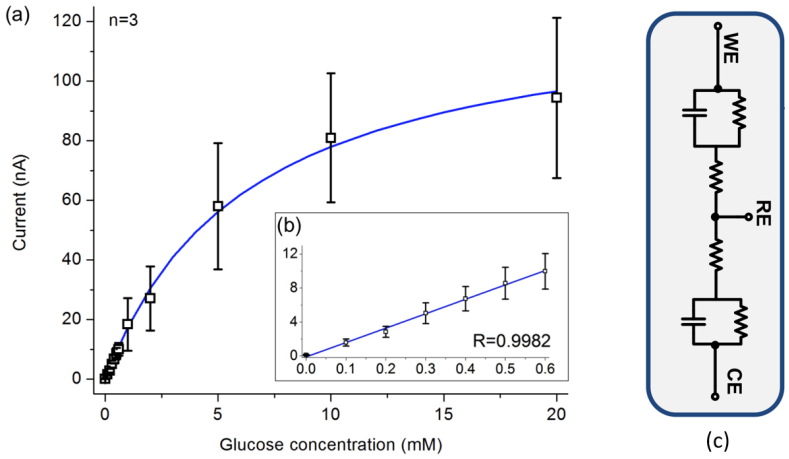

Figure 2.4: The behavior of a glucose sensor: a) sensor generated current up to 20mM; b) sensor generated current up to 0.6mM; c) electric equivalent circuit model of a three-electrode system [27] [28].

Figure 2.4a shows the relationship of current and glucose concentration up to 20mM, and Figure 2.4b is the same response in the 0.1mM to 0.6mM concentration range, which is the expected amount found in human tear. The amperometric current is dependent on the active area of the glucose sensor on the working electrode, and the sensitivity of the sensor. This means that the current range is controllable by carefully designing the sensing element, which can be simplified as a series of linear components as shown in Figure 2.4c: the resistors represent the conductive loss of the metallic electrodes, contact resistance of the interface between the working electrode and the sensor, and the conductive loss of the ionic solution amongst other electrically resistive barriers in the path between the terminals of the working electrode (WE) and the counter electrode (CE); the capacitors represent the interface between the electrode and the solution, as well as the material composition of the sensor. For the correlation reported in Figure 2.4, the reported sensing area is $0.22mm^2$, and the glucose sensitivity is $0.18uA \times mm^{-2} \times mM^{-1}$ [23]. With conservative margins on the concentration of glucose, the graph indicates that the amperometric current would be no more than 20nA.

It is reported in [28] that a 10-bit differential sigma-delta ADC is sufficient to digitize the amperometric current with an approximate 1nA resolution, which is enough for discriminating glucose concentration commonly found in tear.

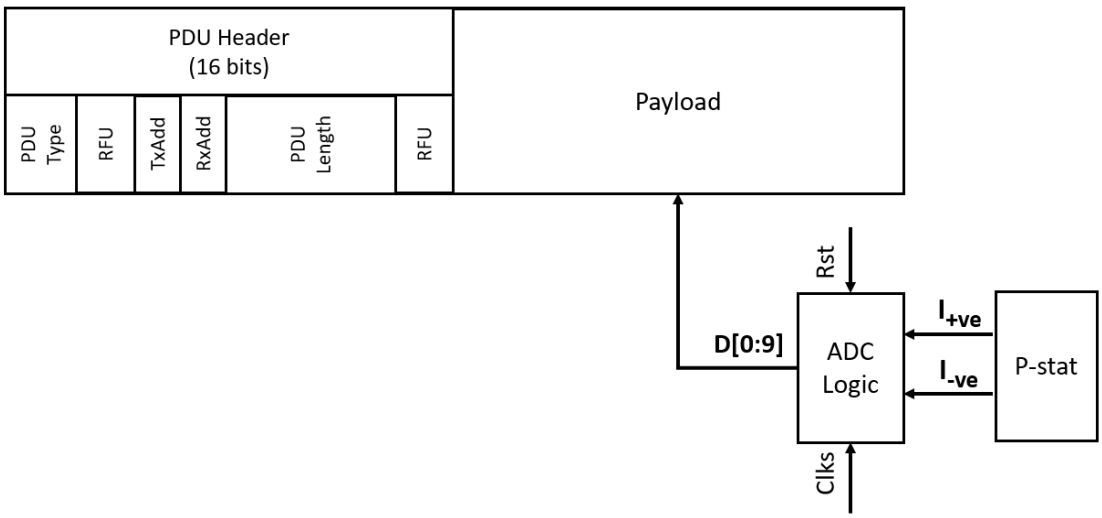

Figure 2.5: Structure of a BLE payload with digitized glucose measurement.

The PDU of a BLE frame from Figure 2.2 is shown in bit-level details in Figure 2.5. The properties of the PDU is characterized by 16 bits to define:

- PDU type: a constant for devices in broadcaster mode (bx000010)
- RFU: reserved for future use bits (bx00)
- TxAdd/RxAdd: address indicator for more advanced payload structures (bx0)
- PDU length: the number of bits of the total PDU

The PDU header can be constructed as a collection of read-only registers, because the structure of the payload does not change in type or length. The values of the payload can be simply interfaced directly from the output of the ADC as a 10-wire connection. Lastly, the PDU must be used as input for generating a 24 bit CRC as specified in the Bluetooth Core Specification documentation. This is a standardized process in digital communication conducted by a linear feedback shift register (LFSR) circuit. Since the preamble and access address are also always a constant value as indicated in Figure 2.2, the end-product of the BLE baseband can be generalized as a short fixed-length burst of binary data in a significantly longer fixed-length idling interval.

2.2 Decisions on the Use of Relevant Frequency Bands

Cellular, Bluetooth, and Wi-Fi are activated on the smartphone as demonstrated in Figure 2.6, before the smartphone is brought close to the smart contact lens. It is expected that the lens will harvest energy from the cellular emission to sustain operation of the on-lens microelectronics for glucose measurement and wireless data communication; while the lens is powered, Wi-Fi and Bluetooth will work together to enable radio backscattering of on-lens glucose data to the smartphone.

2.2.1 Targeted Frequency for Energy Harvester Design

The energy harvester is made to take advantage of the cellular radio rather than radio used for personal area networks, due to the higher upper bound in output power. Smartphones emit between 18dBm to 33dBm of power depending on the utilized radio network (2G/3G/4G), board design, and antenna efficiency [29]. 2G GSM is chosen as the RF source for energy harvesting on the smart contact lens, due to the availability of 2G-enabled smartphones with 30dBm or higher Total Radiated Power (TRP), and low-cost test equipment for conducting measurements on the energy harvester prototype. Depending on the region

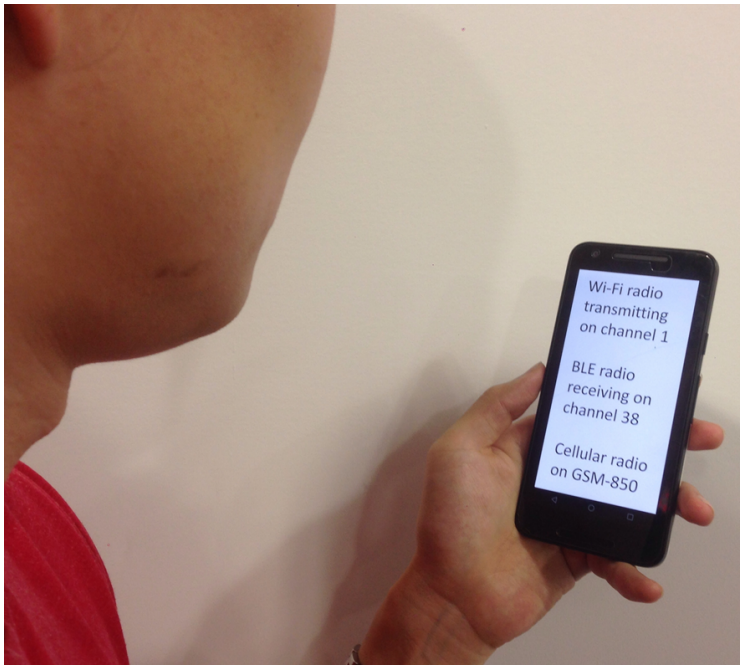

Figure 2.6: The smart contact lens taking advantage of GSM, Wi-Fi, and Bluetooth radio on a smartphone.

around the world, GSM covers over a dozen different frequency spectrum bands from 824-MHz to 1990-MHz, which include both the Uplink and Downlink bands. Uplink bands are of interest here, because the strongest cellular emission close to the smart contact lens would be generated by the smartphone instead of the base-station. Thus, the appropriate frequency bands for the energy harvester design are discriminated down to GSM-850 Uplink band (824.2-MHz to 849.2-MHz) and PCS-1900 Uplink band (1850.2-MHz to 1909.8-MHz), which are used in North America. Under 2G GSM telecommunication, the smartphone automatically picks between either GSM-850 or PCS-1900 depending on its interaction with the surrounding cellular base-stations. For example, Canada uses PCS-1900 as the primary band for urban areas, while keeping GSM-850 as a backup for urban areas and primary for rural areas [30]. The suitability of GSM-850 and PCS-1900 as a RF source for smart contact lens depends on engineering trade-offs due to the frequency difference, which will be investigated during the development of the energy harvester.

2.2.2 Targeted Frequency for Backscatter Design

While the smartphone's 2G emissions are utilized as a power source via energy harvesting, the emission from the smartphone's Wi-Fi channel is used as a backscatter source, and a Bluetooth advertisement channel used to receive the backscattered signals to acquire data from the contact lens.

A critical caveat is that the BLE baseband, framed with glucose payload, cannot directly be used as the modulating signal, because of the monostatic nature of the backscatter architecture (when the smartphone is used as both the backscatter source and receiver): the high powered Wi-Fi signal would dominate the backscattered BLE signal from the contact lens by orders of magnitude, causing significant self-interference. The solution is to use a sub-carrier to bring the BLE baseband frequency to an intermediate frequency, before allowing the signal source from the smartphone to upshift the BLE frame into RF spectrum via backscattering. The choice of frequency for the sub-carrier is the primary reason for the involvement of both BLE and Wi-Fi in this backscattering system.

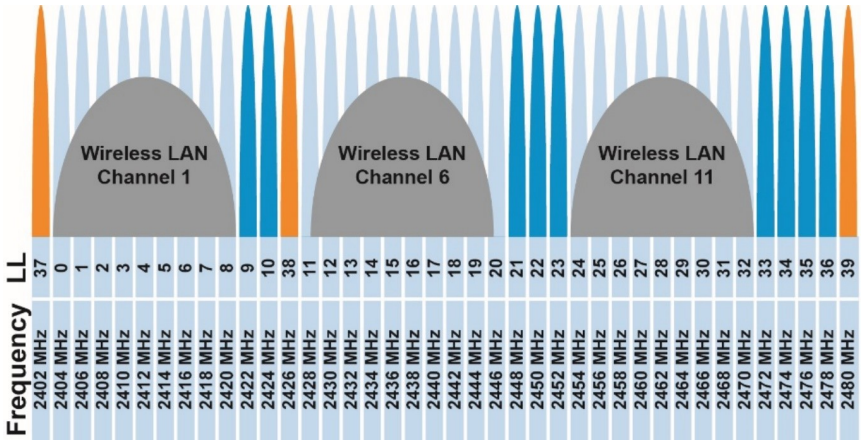

Figure 2.7: Simplified view of frequency assignment of Wi-Fi and Bluetooth channels.

Figure 2.7 depicts the channel assignment of the 2.4-GHz ISM band for some of the commonly used BLE and Wi-Fi channels. By choosing an intermediate frequency of 14-MHz, a deliberate continuous single-tone signal from Wi-Fi channel 1, at 2412-MHz, can be used as an RF source to upshift the BLE frame to an appropriate Bluetooth channel (i.e. advertisement channel 38: 2426-MHz) for detection. Although Bluetooth and Wi-Fi theoretically can occupy the same spectrum simultaneously, Bluetooth features an adaptive frequency hopping mechanism that avoids occupied frequencies, which allows both protocols to operate concurrently, as long as the assigned channels are vacant [31]. This

is also the rationale for choosing the intermediate frequency of 14-MHz, because it avoids overlapping between Bluetooth and Wi-Fi.

2.3 On-Lens Power Specification

Figure 2.8 depicts a block diagram showing the implementation of some of the critical components for the smart contact lens' microelectronics, as well as a smartphone's radio features to support the lens' functionalities.

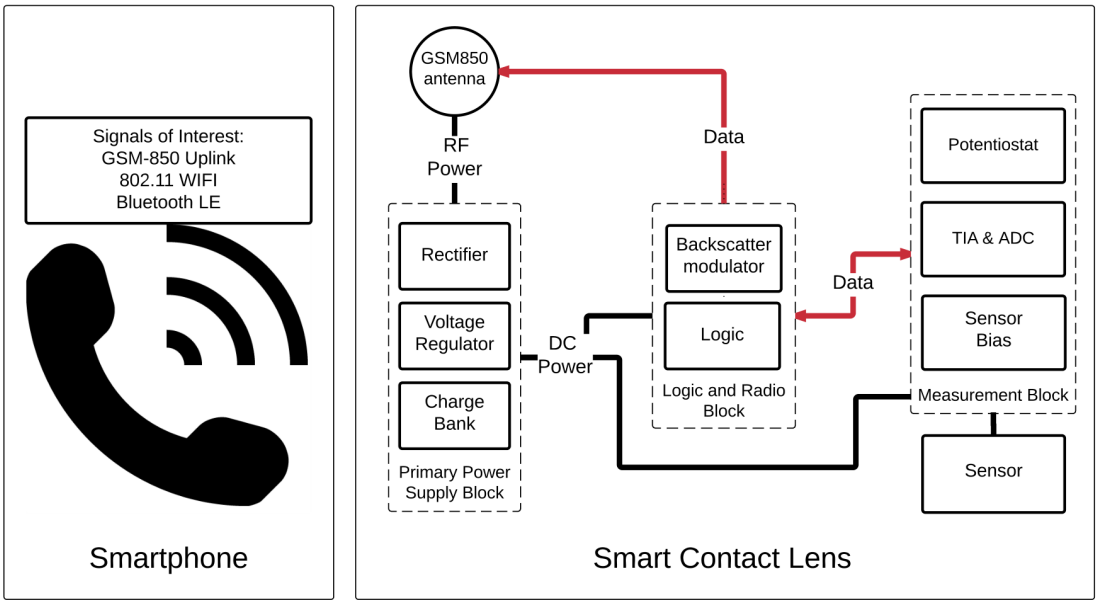

Figure 2.8: Block diagram of relevant on-lens microeletronics in relation to the smartphone.

The "Primary Power Supply Block" is the energy harvester that provides DC power to operate both wireless telecommunication of data and measurement of glucose in the tear. The performance of the energy harvester is designed to meet the DC power consumption requirement of the smart contact lens, which is estimated based on some of the main energy consuming components for communication and measurement.

The "Measurement Block" is intended to convert glucose level to digital data: a potentiostat sustains an amperometric reaction on the sensor; a Transimpedance amplifier converts the amperometric current to an analog voltage level, which the ADC further converts to digital signal. From related works, low power potentiostat circuits—some specifically for

glucose measurement—are designed in commonly found 130nm, 180nm, and 350nm CMOS processes. The generally observed level of power consumption is in the order of 10s of microwatts to 100s of microwatts [32][33][34][35]. Likewise, ADCs built for low power glucose sensing applications are fabricated in similar CMOS processes with a power consumption in the sub-100uW range [36][37][38].

The "Logic and Radio Block" is intended to support the functions of the backscatter module and other digital logic. Digital application-specific IC will define the logic circuitry used to frame the measured glucose data into the BLE packet on a baseband level. The backscatter modulator relies on an oscillator to generate a sub-carrier, and a RF switch to modulate the Wi-Fi signal. Both components have low power CMOS implementations in the sub-100uW range [39][40][41].

The overall DC power consumption of the smart contact lens is estimated to be 1mW, by referencing existing technology for each of the required functional blocks expected in the smart contact lens.

Chapter 3

Energy Harvesting From Cellular Radio Emission on Smart Contact Lens

In this Chapter, the focus is to determine the relationship between the smartphone and the energy harvester, where 1mW of DC power can be generated.

3.1 System Definition of a Rectenna

Energy harvesting from RF sources has been demonstrated as an antenna array with a common rectifier, and as an array of rectenna (rectifying antenna) elements. A rectenna element is usually made of a receiving antenna, a microwave filter, a rectifier circuit, and a dc output filter. The microwave filter acts as an impedance matching network between the antenna and rectifier. The rectifier is a network of cascaded nonlinear circuits, which converts an RF input signal into multiple spectral components at its output including DC, fundamental frequency, harmonics of the fundamental, and possible mixed products due to intermodulation. The rectifier is commonly constructed with zero-bias Schottky diodes or low-power diode-connected CMOS devices in low-power energy harvesting applications. The output filter is a low-pass filter that rejects high frequency harmonics generated by the rectifier during RF to DC conversion. The DC power combines at a common node between all of the array elements to drive a shared resistive load. Although the resistive load is not strictly a component of the rectenna, its resistance value has a significant impact

on the rectenna behavior. The key parameters of an rectenna element are RF power at the terminal of the antenna (received RF power), RF power at the input of the rectifier after transmission from the antenna (available RF power), and DC power after rectification at the load (available DC power). These terminologies for describing power at different locations of the energy harvester are shown in Figure 3.1, and they will be used throughout this thesis.

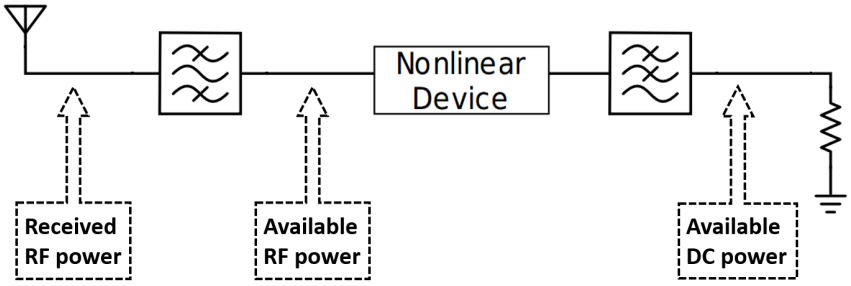

Figure 3.1: A rectenna represented by a general block diagram.

The RF-to-DC conversion efficiency of a rectenna element is influenced by four factors:

1. Antenna efficiency—defines the received RF power
2. Impedance match between the antenna and the rectifier—defines the available RF power
3. Power loss of the rectifier
4. Impedance match between the rectifier and its interfacing load circuits—defines the available DC power

A rectenna is intended to be designed for a well-defined fixed operating point in frequency, load, and available RF power. Optimization must be conducted on all four factors to maximize the overall efficiency of a rectenna. However, the exact power level of the RF source is not a constant parameter in realistic RF energy harvesting applications. Thus, Equation 3.1 conveys the RF-to-DC conversion efficiency of the rectifier by defining it as the ratio of available DC power (P_{DC}) for a specific load, to the available RF power (P_{RF}) at the rectifier input terminal.

$$\eta = \frac{P_{DC}}{P_{RF}} = \frac{V_{out}^2}{R_{load} * P_{RF}} \tag{3.1}$$

With a known resistive load (R_{load}), P_{DC} can be calculated based on the resistance and voltage at the load. Using this definition of efficiency for optimization, it is possible to categorize the research of energy harvesting into antenna design, rectifier circuit design, and integration of the two by impedance matching.

3.2 Antenna for the Smart Contact Lens Rectenna

It is mentioned that the frequency bands of interest for energy harvesting are between GSM-850 Uplink band (824.2-MHz to 849.2-MHz) and PCS-1900 Uplink band (1850.2-MHz to 1909.8-MHz). Both bands have relatively narrow bandwidth compared to their center frequency, which can be accommodated by simple antenna designs such as dipole and loop structures as shown in Figure 3.2.

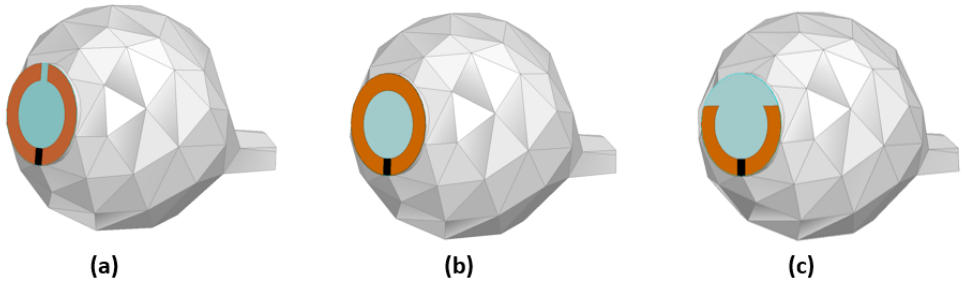

Figure 3.2: Simplified smart contact lens antenna designs in the HFSS simulation environment: (a) GSM-850 dipole; (b) GSM-850 loop; (c) PCS-1900 dipole.

3.2.1 Evaluation of Antennas in Simulation

The antennas are designed in a full-wave simulation software (HFSS) with intensions of determining the most suitable antenna type and operating frequency for energy harvesting on a smart contact lens. The antenna could only be implemented around the outer perimeter of the pupil, which gives the designs in Figure 3.2 a visual commonality. The advantage of using a dipole design like in Figure 3.2a and Figure 3.2c on a contact lens comes from the fact that the arms of the dipole antenna are free to conform to the hemispherical-shape of the eye. An alternative loop antenna design depicted in Figure 3.2b is considered to add elements of comparison in the analysis. All simulation structures are excited in the same manner via a 50ohms lumped port as indicated by the black squares in Figure 3.2.

Both the conductor models and the dielectric models are simplified, because the antenna designs are structurally simple, and it is also difficult to replicate the complexity of the real eye. The simulation-eye is composed of a homogeneous material—the vitreous humor; the antenna is made flat, instead of following the hemispherical-shape of the eye; a 25um polyethylene layer is inserted as a substrate between the antenna conductor and the simulation-eye, which prevents the conductivity of the simulation-eye from distorting expected antenna behaviors.

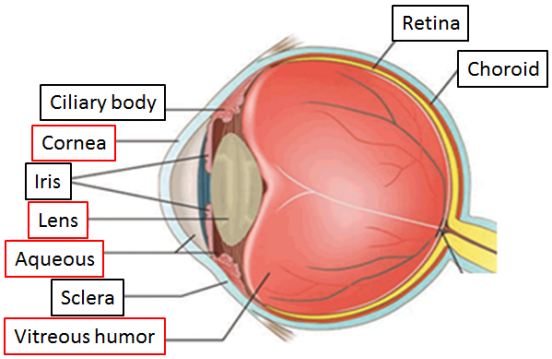

Figure 3.3: Simplified overview of the tissue composition of a human eye.

Table 3.1: Dielectric properties relevant to the smart contact lens under a 830-MHz excitation.

Media	Conductivity [S/m]	Relative permittivity	Loss tangent	Wave-length [m]
Air	0	1	0	0.361
Cornea	1.36	55.51	0.53	0.046
Aqueous Humor	1.5	65	0.5	0.04
Lens	0.77	46.71	0.36	0.052
Vitreous Humor	1.61	68.92	0.51	0.042

A real human eye is a complex organ composed of over a dozen different tissues and organic compounds, where four of them make up majority of the overall mass—namely, the cornea, aqueous humor, lens, and vitreous humor as shown in Figure 3.3. The cornea is the most outer surface of the eye. The smart contact lens floats in-between thin films of tear fluid on the cornea. There is no air or bone in the makeup of the eye. The electric

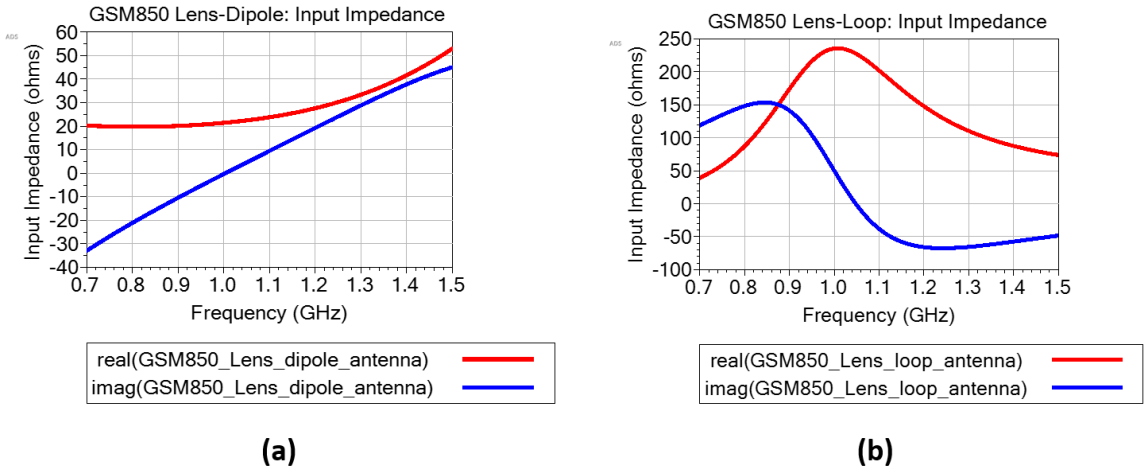

Figure 3.4: Input impedance of the lens antennas for GSM-850 band.

characteristics of the major eye components at 830-MHz are summarized in Table 3.1. Relative to air, organic tissues have similar high conductivity, relative permittivity, and loss tangent. This observation reinforces the validity of using a homogeneous simulation-eye for antenna design in HFSS.

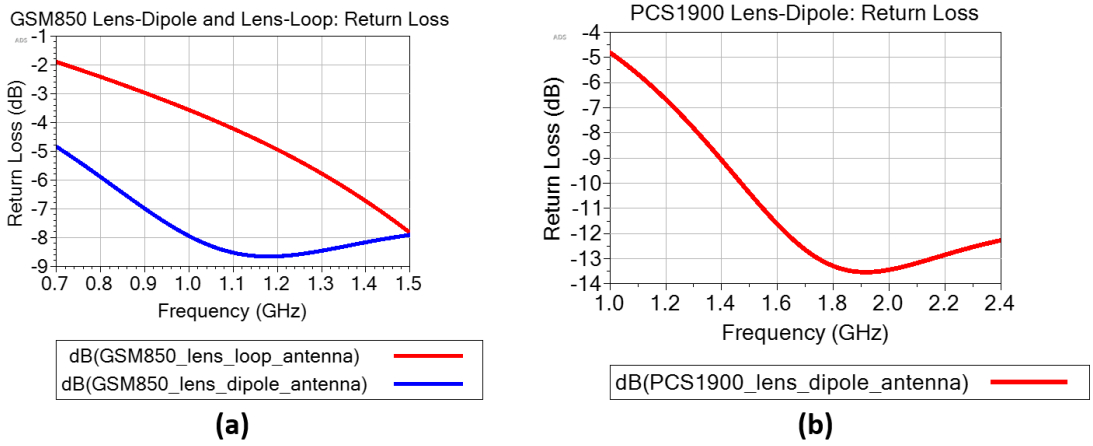

Figure 3.5: Return loss of the lens antennas for GSM-850 and PCS-1900 band.

From Table 3.1, it can also be noted that the 830-MHz wavelength is much shorter on the surface and inside the eye tissues than the wavelength in air, due to the higher relative permittivity. This fact is advantageous to the antenna design, because it facilitates the

design of an efficient resonant antenna by reducing its electrical size.

The HFSS simulation results of the models in Figure 3.2 reflect the effect of the eye has on the antenna structures. The GSM-850 lens-dipole has a natural resonant frequency at 1000-MHz as shown in Figure 3.4a, which is slightly higher than the intended center frequency of the GSM-850 Uplink band. This is caused by the fact that the arms of the GSM-850 lens-dipole cannot be made long enough around the contact lens perimeter to complete a true half-wave structure. The resulting penalty to the return loss is apparent in Figure 3.5a. This issue does not affect the PCS-1900 lens-dipole as seen in Figure 3.5b, because its half-wave structure is within the dimensional constraint of the contact lens. On another hand, the GSM-850 lens-loop produces an anti-resonant frequency close to the GSM-850 Uplink band as shown in Figure 3.4b, which causes a much poorer return loss as compared to the dipole structure.

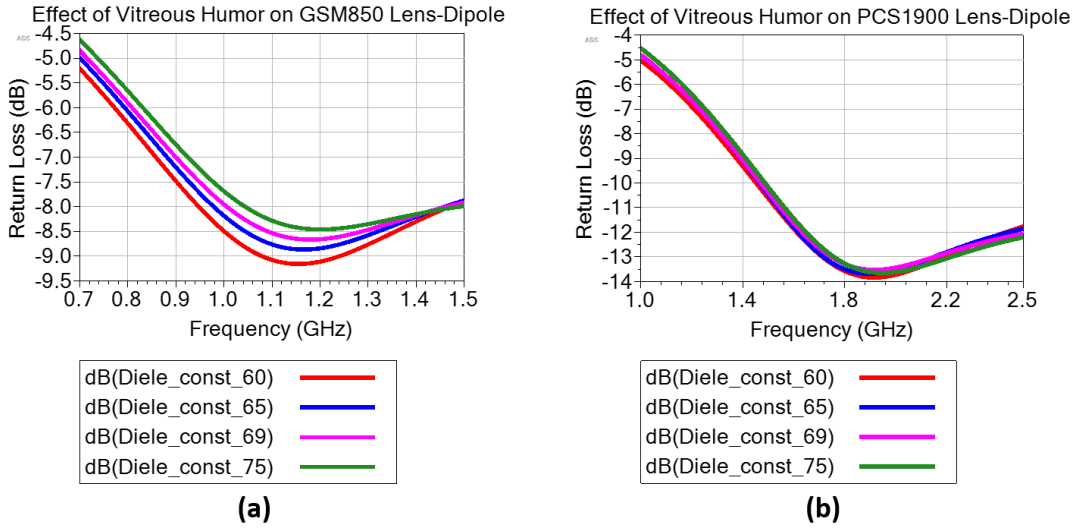

Figure 3.6: Effect of tissue variation on return loss of the lens-dipoles.

The dielectric constant of the homogeneous simulation-eye is varied based on statistic variation of the dielectric constant that could be observed in human eye [42]. Figure 3.6 shows the result of the simulated return loss, which seem to indicate that the lens-dipole is more sensitive at the GSM-850 frequency band than PCS-1900. A closer look at the axis-scale reveals that both antennas experience an approximate 0.5dB of variation at their respective resonant frequency.

Figure 3.7 shows a stripped-down version of a human head simulation model, which is used in HFSS to replicate a more comprehensive dielectric environment than the standalone

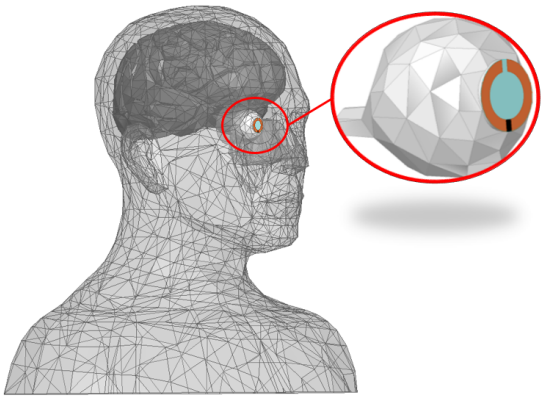

Figure 3.7: A simplified head model and eye model in the HFSS simulation environment.

eye model. This simulation-head model includes a brain and skin, which are the most fluid-filled tissues close to the eye. The same antenna models in Figure 3.2 are inserted in a cavity made on the simulation-head model. The simulation results comparing the differences made by the head and that of the eye are shown in Figure 3.8 and Figure 3.9.

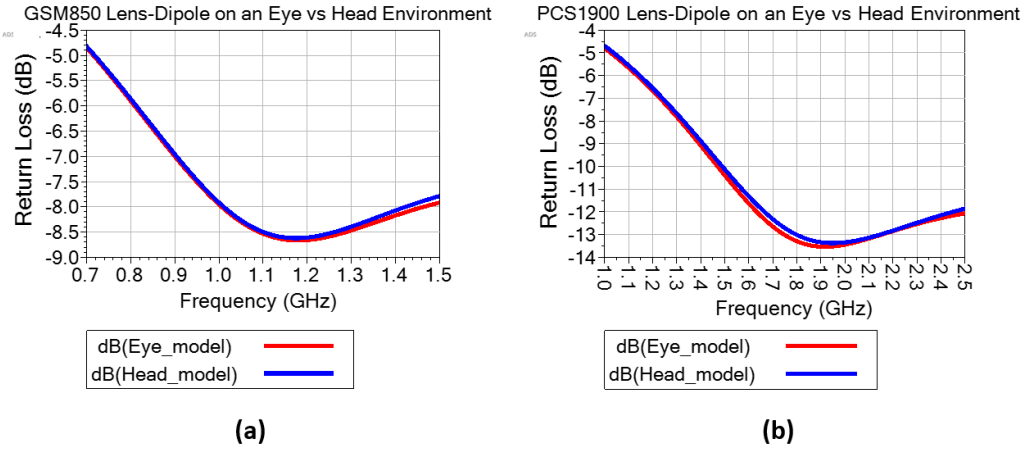

Figure 3.8: Effect of head model on return loss of the lens-dipoles.

Figure 3.8 shows that the addition of a simulation-head does not have a significant impact on return loss for a dipole antenna structure at either the GSM-850 band or PCS-1900 band. Although the loop antenna is not shown, it is known that a loop antenna structure is much less sensitive to environmental impact than a dipole antenna.

The real impact of the simulation-head is on the antenna gain pattern. All three

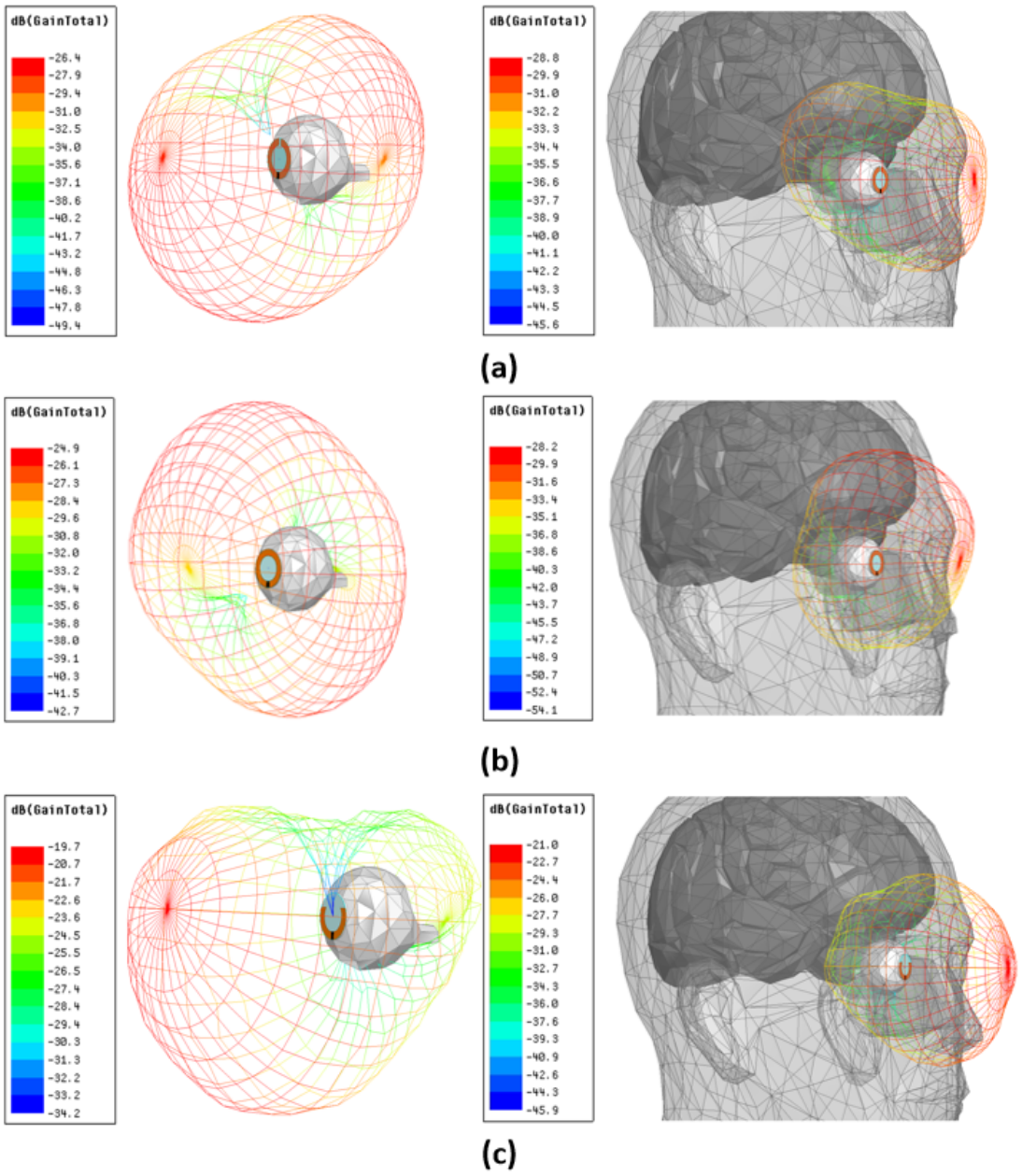

Figure 3.9: Effect of head model on gain pattern of the lens-antenna: (a) GSM-850 lens-dipole; (b) GSM-850 lens-loop; (c) PCS-1900 lens-dipole.

antenna structures are shown in Figure 3.9. The simulation-head absorbs radiation towards the back of the head, but the outward facing gain is only slightly affected at the gain maximum when compared to only a standalone simulation-eye is used for simulation. The gain pattern of the lens-dipoles in Figure 3.9a and Figure 3.9c do not affect the use-case of the smart contact lens application when the smartphone is directly in-front of the lens in the approximate area of the maximum gain. However, the attenuation becomes much more significant in the case when the smartphone is placed beside the human ear (e.g. when the phone is used during voice-call). On the other hand, the gain pattern of the lens-loop in Figure 3.9b may affect both use-cases, because the maximum gain could be in an unpredictable direction when the smart contact lens is worn.

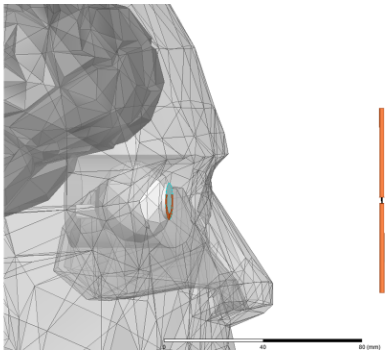

Figure 3.10: Configuration of an insertion loss simulation between a lens-antenna and an acting-antenna for the smartphone.

Figure 3.10 shows the setup to perform insertion loss simulation in HFSS to gain an insight into the amount of power that the smart contact lens can harvest from a smartphone. The simulation-head model from Figure 3.7 is kept, and a wire-dipole (tuned to the appropriate resonant frequency for GSM-850 and PCS-1900) is used to emulate the smartphone because of their shared omni-directional behavior. The wire-dipole is placed at a distance where the smart contact lens antenna can receive the expected power commonly found in RF energy harvesters.

The insertion loss of all thee antenna are compared in Figure 3.12 under the condition that the return loss of the antenna are well matched as shown in Figure 3.11a and Figure 3.11b. It is observed that the GSM-850 lens-loop has the best performance at 42dB of insertion loss. However, considering its marginal gain in performance compared to the GSM-850 lens-dipole, other factors such easy of integration and packaging make the GSM-850 lens-dipole a more practice antenna structure for the smart contact lens. If a smartphone is transmitting at the maximum TRP of 33dBm, the smart contact lens can

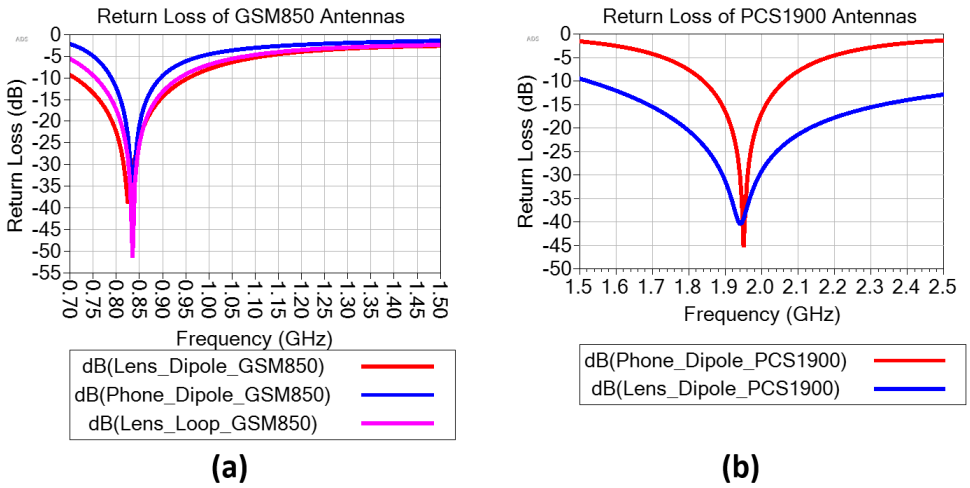

Figure 3.11: Return loss of (a) antennas for GSM-850 band, and (b) antenna for PCS-1900 band.

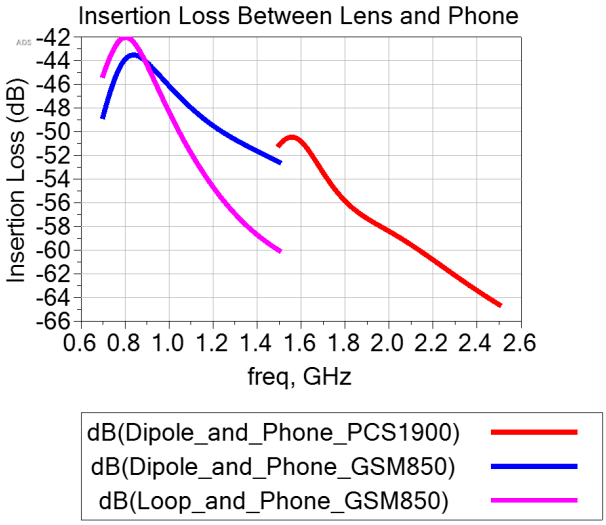

Figure 3.12: Insertion loss of antennas for the GSM-850 band, and the PCS-1900 band.

expect a maximum received RF power of -11dBm at its antenna terminal. Therefore, the development on the energy harvester circuit is best to utilize a GSM-850 lens-dipole as the preferred antenna and frequency.

3.2.2 Construction of an Antenna Prototype

An electrically realistic eye model is constructed to replicate the effect that the eye has on the GSM-850 lens-dipole antenna. Both are shown in Figure 3.13. The development of a physical model that allows for accurate testing of the proposed energy harvester is a critical aspect of the development process. For this purpose, a method is developed for the synthesis of artificial human eye tissue. It is aforementioned that an eye model with homogeneous material would resemble that of a real eye. Thus, the construction of the realistic eye model here is consisted of a single type of liquid with specific chemical composition held within a thin-walled polyurethane pouch, which is contained in a 3D-printed hollow sphere to represent the sclera (the white outer layer of an eyeball). It has an interior diameter equivalent to the average human eye. An opening at the front of the sclera allows the polyurethane pouch to protrude out like the cornea.

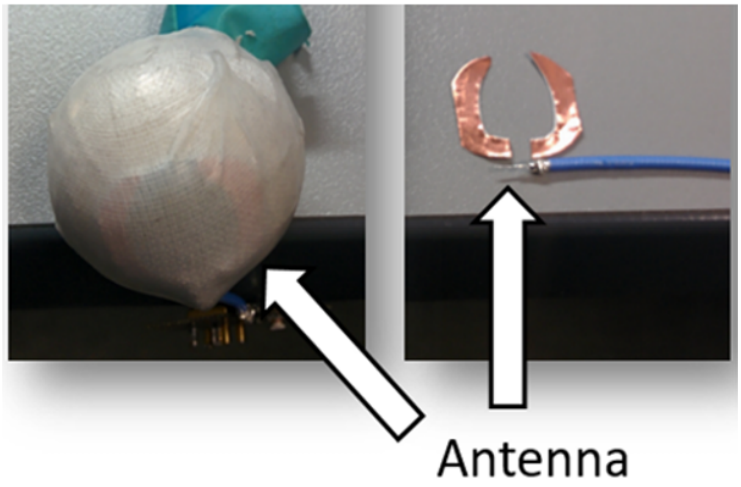

Figure 3.13: Left: eye model with antenna encapsulated behind medical tapes; Right: disassembled planar dipole antenna including coaxial.

A GSM-850 lens-dipole antenna is held in place on the polyurethane cornea using semi-transparent medical tape. The antenna is constructed with hand-crafted planar copper pieces, and its port is fed via a 50ohms coaxial cable. Figure 3.14 shows the natural resonant frequency of this fabricated GSM-850 lens-dipole close to 800-MHz, which is similar to the simulated result in Figure 3.4. The differences in antenna construction likely contributed to the 200-MHz downshift of the resonant frequency compared to that of the simulated result.

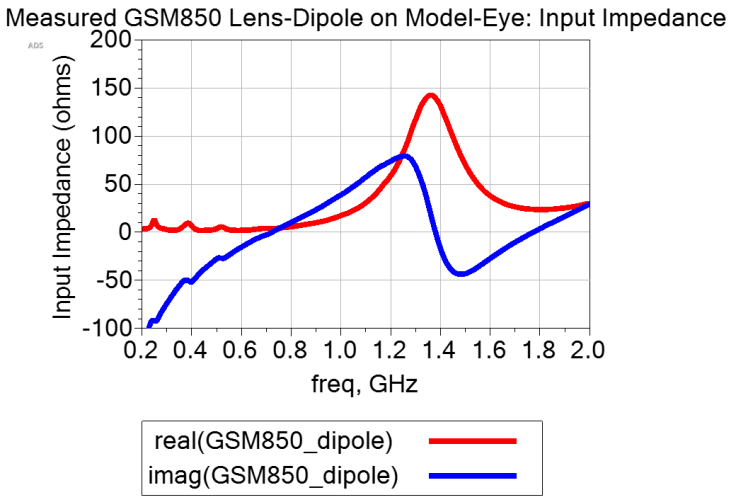

Figure 3.14: Measured input impedance of GSM-850 lens-dipole on the model-eye.

The model-eye requires a specific chemical composition in order to act as an accurate human eye simulant. The vitreous humor, which forms the bulk mass of the eye, also has a DC conductance of 1.5 S/m [43]. A liquid solution is prepared containing a specific composition of water and salt to reach the DC conductance of vitreous humor. Salt (NaCl) is added to deionized water, whilst monitoring the change in DC conductivity using a conductance probe, until a value of 1.5 S/m is reached. 7.5mL (the volume of the average human eye) of this saline solution is placed into the thin-walled polyurethane pouch as shown in Figure 3.13.

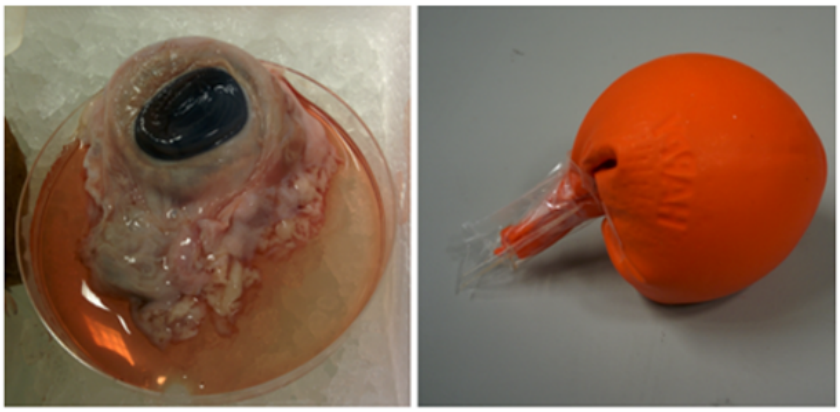

Figure 3.15: Left: a bovine eye; Right: bovine eye in a polyurethane pouch.

Ideally, the material specifications of the model-eye can be determined by comparing the input impedance of the GSM-850 lens-dipole antenna on the model-eye to its input impedance on a human eye. In our experiment, a laboratory bovine eye is employed in place of a human eye as shown in Figure 3.15, because the hand-crafted lens-dipole antenna is too crude to test on a human subject. Note, the lens-dipole antenna would be passivated to avoid making direct contact with moisture in a contact lens. Similar, the bovine eye in Figure 3.15 is encapsulated in a polyurethane pouch to achieve the same objective.

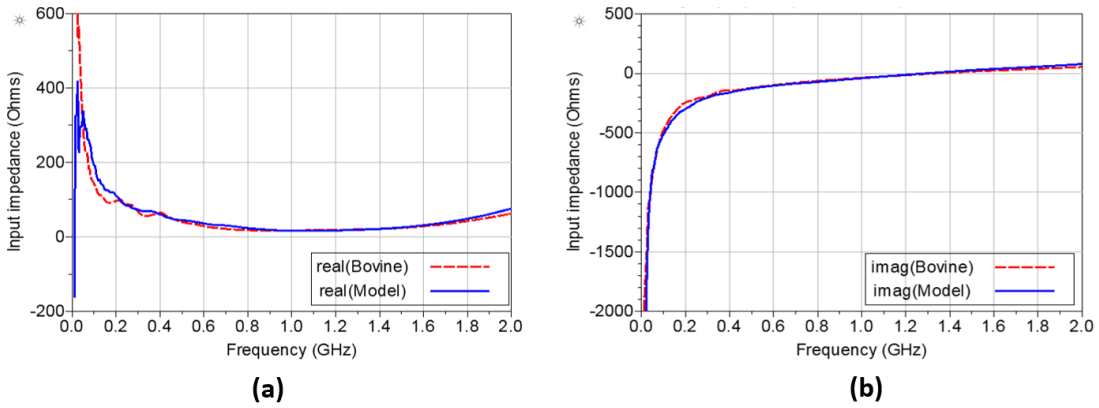

Figure 3.16: Measured input impedance of the GSM-850 lens-dipole on a bovine eye vs the model-eye: (a) real component; (b) imaginary component.

The measured input impedance of the GSM-850 lens-dipole on the bovine eye matches closely with measured input impedance on the model-eye as shown in Figure 3.16. Very similar behaviors of both the real and imaginary impedance for the antenna suggests that the model-eye accurately replicates the electrical properties of a real eye up to at least 2-GHz.

3.2.3 Measurement of Power Captured on the Antenna Prototype From Smartphone

The GSM-850 lens-dipole on the model-eye is adjusted for the GSM-850 Uplink band through impedance matching. A pi-network is used to match the lens-dipole to a 50ohms terminal. The return loss is shown in Figure 3.17. The antenna bandwidth is measured to be 50-MHz from 820-MHz to 870-MHz, which covers the entire GSM-850 Uplink band.

It is found from the simulated insertion loss result in Figure 3.10 that the maximum received RF power at the lens-dipole terminal is -11dBm. To replicate this result in mea-

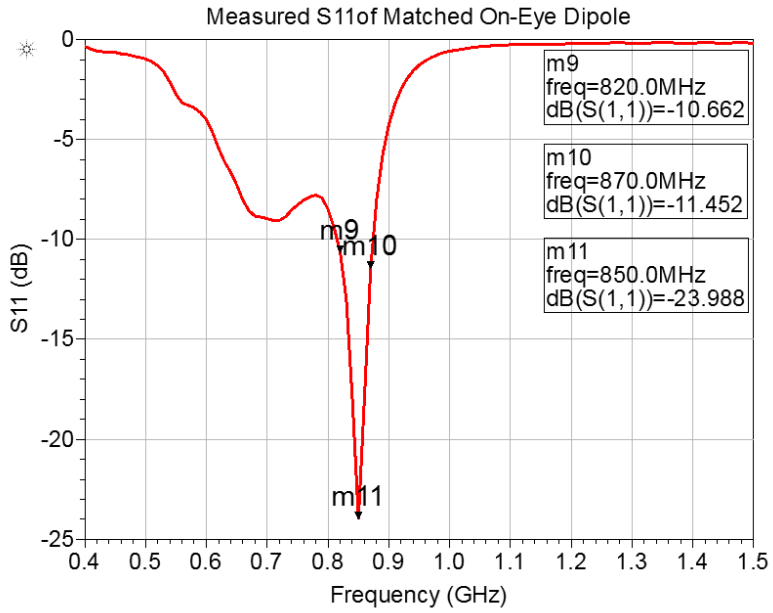

Figure 3.17: Measured return loss of the matched GSM-850 lens-dipole.

surement, the matched GSM-850 lens-dipole is connected to a spectrum analyzer, and the antenna is observed to capture nearly 2dBm from a smartphone's GSM-850 Uplink emission as shown in Figure 3.18b. The smartphone's cellular network setting is restricted to 2G GSM only, and an outbound call is made during the measurement. Figure 3.18a shows the setup of the measurement: the lens-dipole antenna is placed 10cm away from the smartphone when the emission level is captured on the spectrum analyzer.

Figure 3.18b shows two peaks with a very sharp null. This is due to the rapid switching of channels when the outbound call is first made. The base-station eventually finds a fixed available channel for the phone to transmit upon within the GSM-850 network. In this case, the lower frequency peak is at 829.2-MHz, and the higher frequency peak is at 849.2-MHz, which are the near-lowest and highest frequency utilized by the GSM-850 band; they are both within the bandwidth of the antenna as shown in Figure 3.17.

3.3 Rectifier for the Smart Contact Lens Rectenna

It is shown that the measured maximum available RF power is approximately 2dBm when the GSM-850 lens-dipole is in line-of-sight (LOS) and 10cm away from a smartphone. Thus,

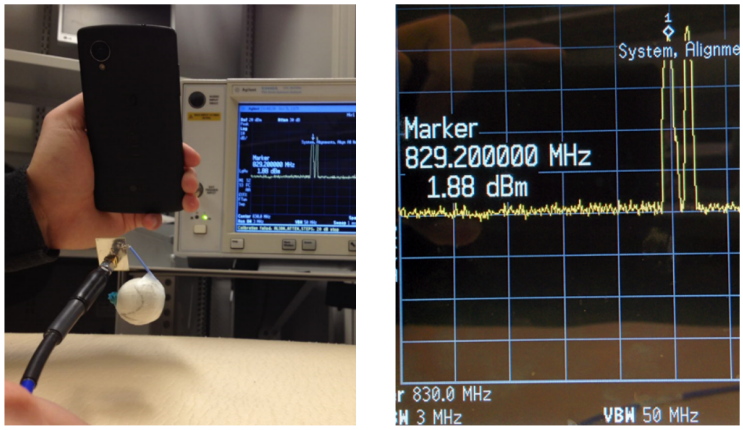

Figure 3.18: Received RF power measured on the GSM-850 lens-dipole on an model-eye: (a) measurement setup; (b) received RF power level from smartphone.

the rectifier on the smart contact lens rectenna is made to capture energy from a single frequency band (GSM-850 Uplink), with the possible available RF power of approximately 2dBm. Also, the targeted upper bound DC power is 1mW at 2V as desired by the power specification of the on-lens microelectronics.

3.3.1 Rectifier Circuit Topologies

Class-D half wave rectifier is commonly found in energy harvesting applications with the characteristics of low input-voltage (as RMS) and high output-voltage (as DC). The voltage doubler shown in Figure 3.19b is an example of a Class-D half wave topology. It utilizes two diodes (or equivalent of diodes): the series diode with respect to the port provides a path for positive source current going to output; the shunt diode provides a path for negative current going back to the source. The capacitors sustain a continuous charging and draining of current via the two diodes, which amplifies the voltage at the output twice the input voltage, and also creates a square wave voltage across the series diode. The drawback of the Class-D topology stems from the fact that the rapid switching of the square voltage waveform causes complete charging and discharging of the capacitors, which leads to loss of power. However, stressing the devices to enable complete flow of current throughout the circuit also leads to high output power capabilities, which is advantageous for applications where the power level at the output is critical.

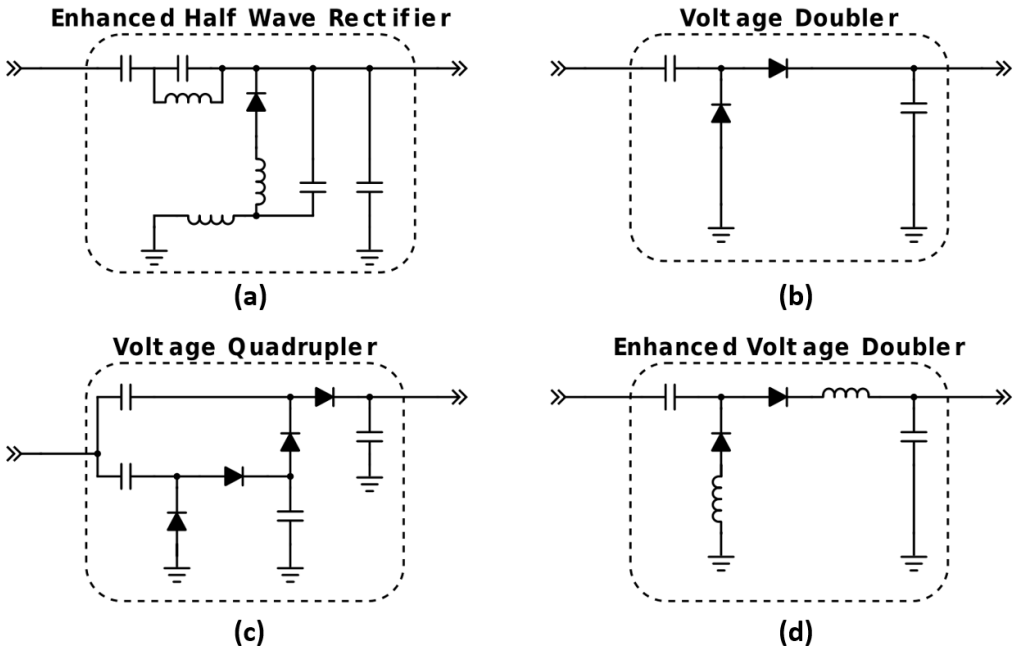

Figure 3.19: Rectifier topologies: (a)enhanced half wave rectifier; (b) voltage doubler; (c) voltage quadrupler; (d) enhanced voltage doubler.

The voltage doubler can be cascaded to achieve a higher multiplication of input voltage at the rectifier output. Figure 3.19c shows a voltage quadrupler (4x multiplication) composed of two stacked voltage doublers with a common input source. There exists an optimal number of cascaded stages to maximize the RF-to-DC conversion efficiency for a specific input power level [44][45][46].

Figure 3.19d shows a modified voltage doubler with additional inductors on the paths of the diodes, and both are added to enhance the RF-to-DC conversion efficiency of the voltage doubler through harmonic termination. The use of harmonics termination in rectifier circuits have been studied to minimize the voltage and current at the harmonics to produce a higher powered DC component at the output of the nonlinear device [47][48].

Figure 3.19a is a single diode half wave rectifier, which is also the simplest rectifier. This configuration acts as a good reference for comparing it against multi-diode topologies in 3.19 by providing insight into the significance of the diode's threshold voltage on increasing loss to the rectifier. Especially in conditions with low available RF power, the rectifier efficiency can be degraded by the diodes internal resistive losses due to the inability to fully turn-on.

3.3.2 Comparison of Rectifier Topologies

Comparison of the rectifier topologies mentioned in Figure 3.19 is made by conducting simulations in Advanced Design System (ADS). As an example, the setup of the enhanced voltage doubler topology is shown in Figure 3.20. The evaluation of the rectifier is simulated as a part of whole the rectenna including the rectifier circuits, the matching network, the resistive load, and a RF power source at the input acting as the antenna. The source has a 50ohms input impedance, and it outputs a single-tone continuous carrier with parameterized operating frequency and received RF power.

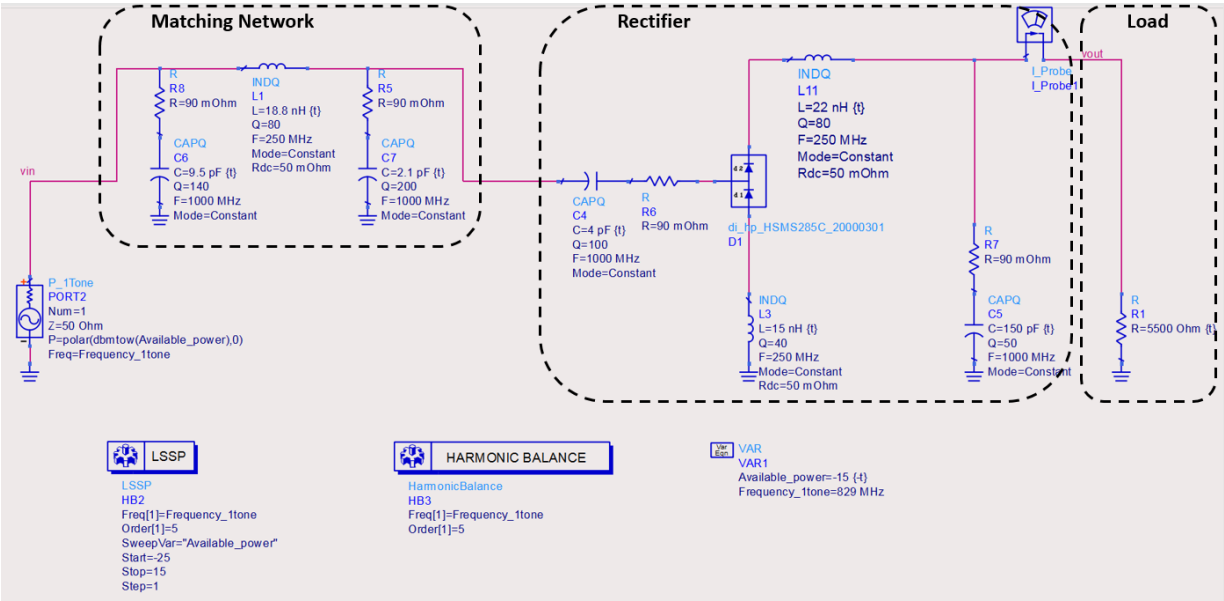

Figure 3.20: ADS circuit schematic simulation of a rectenna with the enhanced voltage doubler topology.

The setup utilizes both the Harmonic Balance (HB) and the Large Signal S-Parameters (LSSP) simulation tools, because the rectification characteristics in a nonlinear device such as a diode behaves in two ways: small signal operation, and large signal operation. HB is used to analyze small signal behavior, where the nonlinear device expands the input signal into many frequency components including the DC component. LSSP is used to approximate the reactive behavior of the circuit to different input power levels, which determines changes in the input impedance of the rectifier. Together, HB and LSSP enable the simulation to predict the RF-to-DC conversion efficiency with respect to the received RF power.

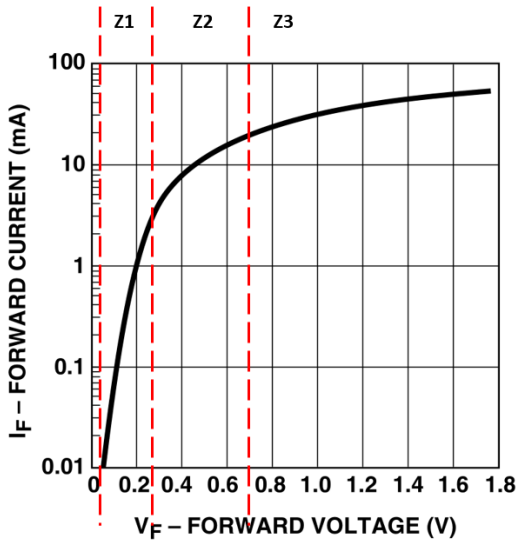

Figure 3.21: IV curve of the diode used in the enhanced voltage doubler circuit [49].

The simulation uses real-world components with model characteristics given by the manufacturers. The capacitors and inductors are defined with a frequency-dependent quality factor and a series resistance. The diode of choice is the HSMS-285C Schottky barrier diode. Although the HSMS-285C datasheet claims that the diode is intended for use with input power less than -20dBm, measured experiments have shown that the HSMS-285C is best for input power up to 5dBm [50]. Since the measured maximum available RF power from the GSM-850 lens-dipole is close to 2dBm, the HSMS-285C is a suitable device for the rectifier design. The current-voltage curve from the HSMS-285C datasheet is shown in Figure 3.21.

HSMS-285C is a zero-bias operating device, and that no externally applied DC power is needed to create a quiescent bias point. The diode becomes self-biased during the RF-to-DC conversion process. The current-voltage curve of the small-signal operation can be classified into three different operating zones as shown in Figure 3.21: Zone 1 (Z1) is the square law zone, where the output signal is proportional to the square of the input signal, which generates the maximum DC component; Zone 2 (Z2) is the transition zone, where the diode starts to loss RF-to-DC conversion efficiency; Zone 3 (Z3) is the resistive zone, where the output signal is approximately proportional to the input signal, and conversion efficiency goes to zero.

In the full ADS simulation environment shown in Figure 3.20, the source power (received RF power) is swept from -45dBm to 15dBm for the rectifier structures shown in Figure

3.19, and the source frequency is at a fixed constant of 830-MHz to cover the GSM-850 Uplink bandwidth.

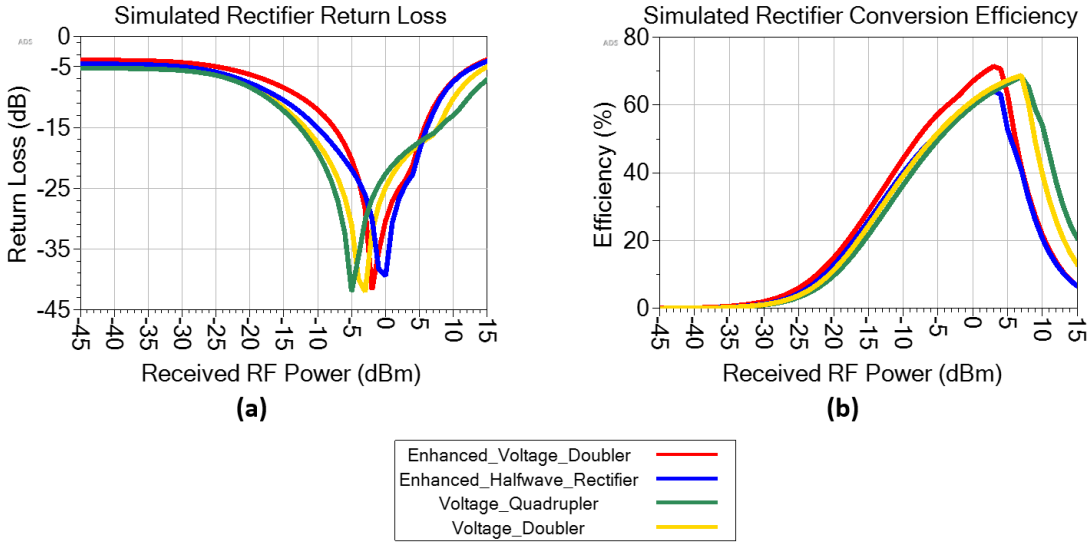

Figure 3.22: ADS simulated rectifier power behavior: (a) RF-to-DC conversion efficiency; (b) return loss.

The RF source impedance must equal the complex conjugate of the input impedance of the rectifier circuit to achieve optimum power transfer. Since the input impedance of rectifier changes with the input power, a conjugate impedance match is only possible for a specific value of input power level, preferably the operating input power level expected for the circuit. Thus, the matching network, resistive load, and component parameters of the rectifier circuit are optimized to match the rectifier for a constant received RF power level between -5dBm to 0dBm, because the power bandwidth of the return loss (defined at -15dB) is relatively wide, and that HSMS-285C performs poorly at input power over the 5dBm limit. It is shown in Figure 3.22a that all four rectifier topologies have an available RF power bandwidth of approximately 20dBm, which covers the upper bound of the HSMS-285C diode.

The RF-to-DC conversion efficiency of the optimized rectenna with different rectifier topologies are calculated based on the definition given in Equation 3.1. The losses from the matching network components are low enough to attribute the RF-to-DC conversion entirely to the rectifier circuit. All four topologies have relatively similar efficiency (within 10%) as shown in Figure 3.22b; the enhanced voltage doubler has the highest efficiency at approximately 70% when 2dBm of Received RF power is provided.

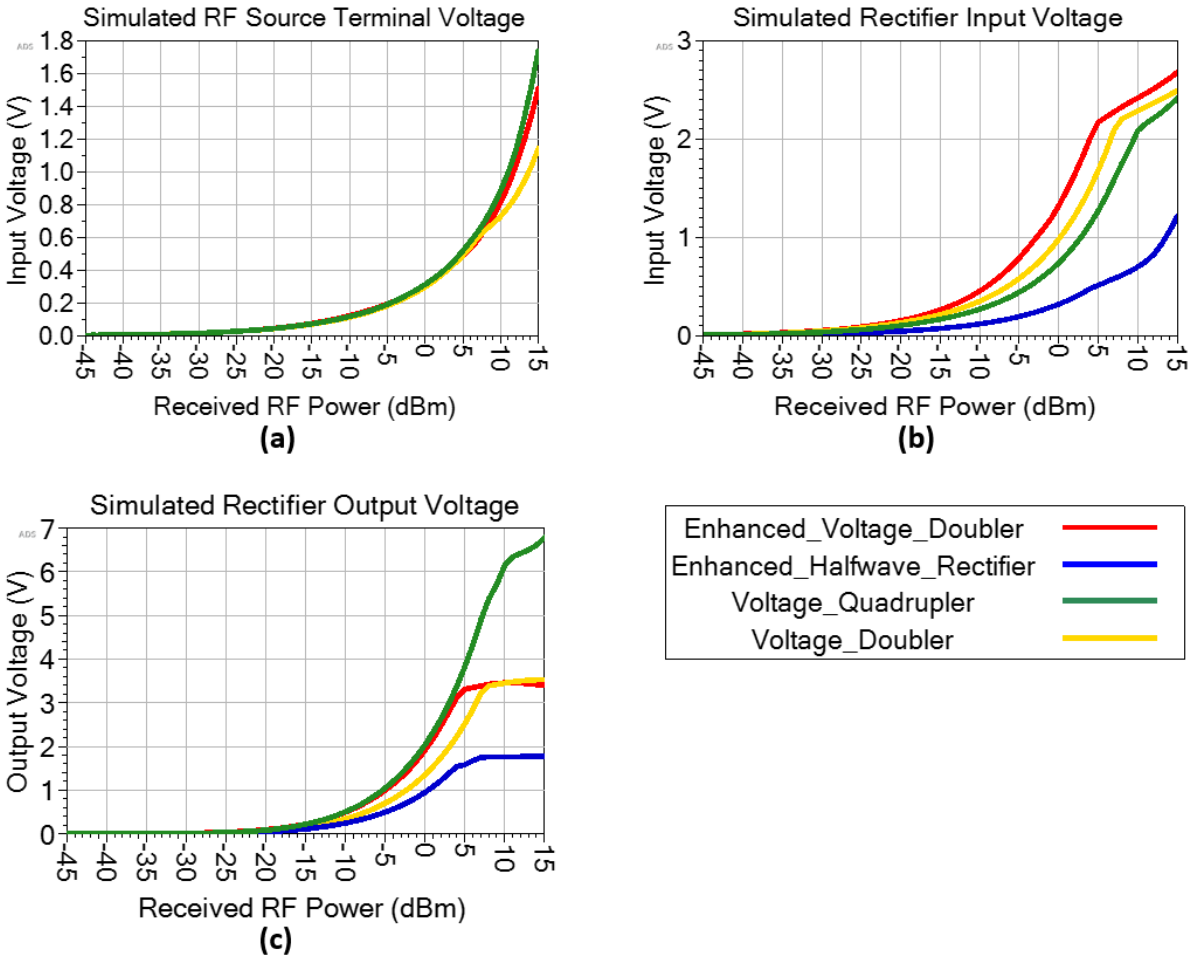

Figure 3.23: ADS simulated rectifier voltage behavior: (a) voltage at the RF source terminal; (b) voltage at the rectifier input terminal; (c) voltage at the resistive load.

when the received RF power is 2dBm, Figure 3.23a shows that all four rectenna structures have similar voltage of 0.4V before the matching network. After the matching network, the voltage at the rectifier input terminal becomes dependent on the component values of the matching network and the input impedance of the rectifier circuit. Figure 3.23b shows the rectifier input voltage. It is difficult to control this voltage level, because the rectenna has a focus on maximizing efficiency by simultaneously adjusting the values of the matching network, rectifier circuit, and the load resistance. Figure 3.23c shows the rectenna output voltage at the load: at 2dBm received RF power, the enhanced half wave rectifier and the voltage doubler are both below the 2V threshold defined as the targeted

operating voltage of the smart contact lens; the enhanced voltage doubler and the voltage quadrupler both satisfy the targeted 2V specification.

Table 3.2: ADS simulated Harmonic Balance result of all four rectifier topologies.

Frequency	Enhanced Voltage Doubler	Half Wave Rectifier	Voltage Doubler	Voltage Quadrupler
0-Hz	0.5 dBm	0 dBm	0.1 dBm	0 dBm
829-MHz	-63 dBm	-9 dBm	-60 dBm	-66 dBm
1658-MHz	-72 dBm	-48 dBm	-69 dBm	-75 dBm
2487-MHz	-80 dBm	-58 dBm	-78 dBm	-84 dBm
3316-MHz	-80 dBm	-58 dBm	-78 dBm	-84 dBm
4145-MHz	-80 dBm	-55 dBm	-80 dBm	-89 dBm

Table 3.2 shows that the four rectenna structures all have their respective DC power above the 1mW (0dBm) threshold as targeted for the smart contact lens to operate. The enhanced voltage doubler generates the highest DC power from a 2dBm received RF power. The additional inductors in the circuit created weaker fundamental and harmonic frequency components than the standard voltage doubler. The enhanced half wave rectifier has the highest power in its fundamental and harmonic frequencies, but the output DC power is still on the same level with the voltage multipliers. This is due to the advantage of using only a single diode, which decreases the resistive loss that diodes can cause to the rectifier circuit.

Table 3.3: Optimial load resistance for the ADS simulated rectifier topologies.

	Enhanced Voltage Doubler	Half Wave Rectifier	Voltage Doubler	Voltage Quadrupler
Load Resistance	5500 Ω	1500 Ω	3000 Ω	7000 Ω

On the otherhand, the voltage quadrupler has an output DC power of 0dBm dispite having the highest voltage, because it is driving a higher resistive load than the other rectifier topologies as shown in Table 3.3.

3.3.3 Construction of the Rectifier Prototype

The enhanced voltage doubler rectifier topology from Figure 3.20 is selected for fabrication and measurement as a PCB implementation. The PCB is designed in a mixed simulation environment, where the PCB structure is characterized in a full-wave simulation software (HFSS), and its effect is simulated alongside the lumped component SPICE models in ADS.

Figure 3.24a shows the PCB layout in HFSS, which is constructed to realistically mimic the geometries and material properties of the PCB for fabrication: 0.8mm thick FR4 is used as substrate, 0.5oz copper cladding is used as conductor for the microstrip circuit, manufacturer recommended footprints are used for components, and 50ohms transmission line is used to connect the components, because the PCB is intended to interface with the GSM-850 lens-dipole antenna via a 50ohms SMA connector.

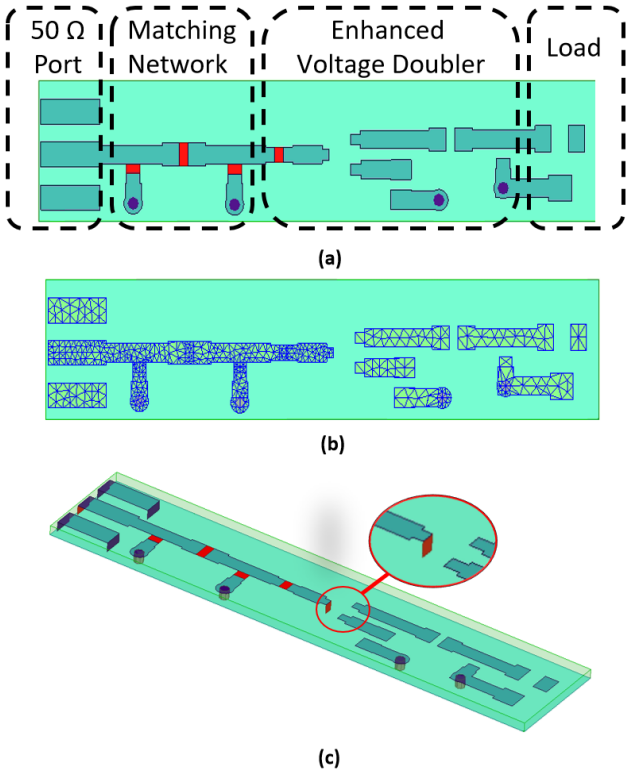

Figure 3.24: HFSS simulated enhanced voltage doubler structure: (a) circuit layout; (b) mesh density distribution of the structure; (c) lump port placement on the structure.

In HFSS, 50ohms lump ports (marked in red color in Figure 3.24c) are used in place of RLC components, terminal of the SMA connector, and the common terminal joining the Schottky diodes—the HSMS-285C is in a SOT-323 Package, where the diodes are connected in series. This multiport S-parameter analysis is conducted with a focus on ensuring a well-matched impedance between the diodes and the antenna. It can be observed in Figure 3.24c that only some of the components are represented by lumped ports in HFSS, because the input impedance of the HSMS-285C is mainly affected by SPICE models in ADS. Thus, the HFSS simulation only needs to consider the components between the diodes and the SMA connector, which reduces the simulation size as seen by the distribution of mesh density in Figure 3.24b.

Figure 3.25 depicts the ADS simulation environment. The 6-port S-parameter result from HFSS is imported to ADS as a data file block that connect the input port, the matching network, as well as the diodes and the subsequent lumped components following the diodes. Microstrip-line blocks are introduced between components to compensate for the missing transmission lines due to a simplified HFSS simulation. A combination of HB and LSSP tools is used in a manner described in the full ADS simulation environment shown in Figure 3.20.

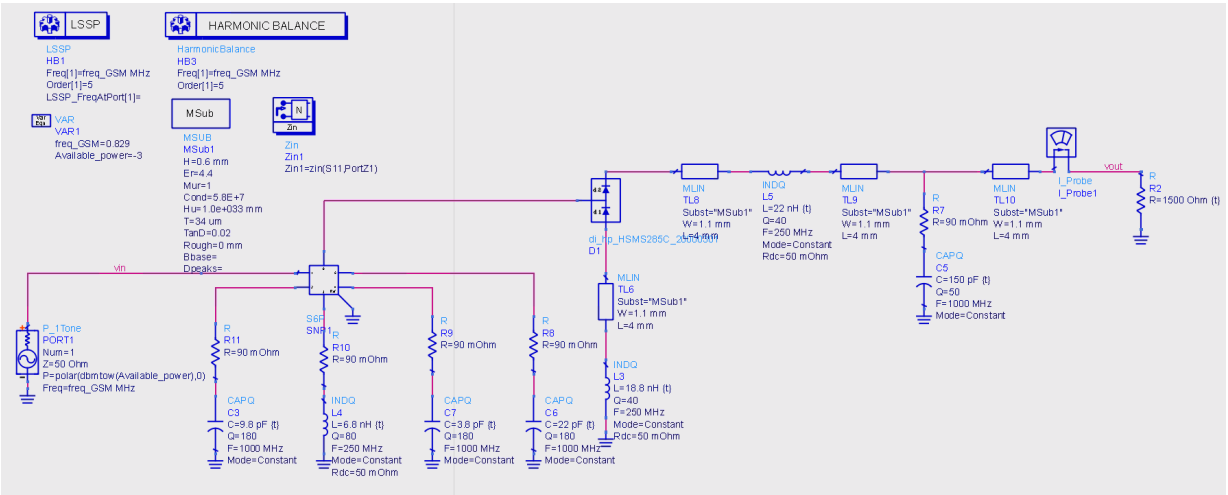

Figure 3.25: ADS circuit schematic simulation with HFSS simulated S-parameter of the enhanced voltage doubler PCB layout.

Figure 3.26 describes the effect of the quality of the RLC components and PCB have on the RF-to-DC conversion efficiency in the simulation configuration of Figure 3.25. The Lossless configuration involves changes in both the HFSS and ADS simulation: tangent

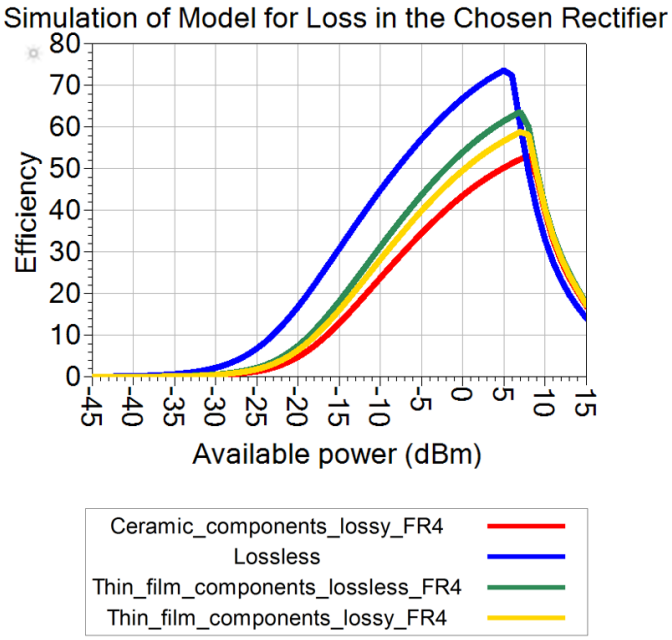

Figure 3.26: Component and PCB loss evaluation from combined ADS and HFSS simulation.

Figure 3.27: The fabricated enhanced voltage doubler with matching network and load.

loss of the FR4 is set to zero for the PCB in HFSS; inductors and capacitors are given high quality factor and no series resistance. The conversion efficiency is very sensitive to component properties, as seen by an approximately 10% decrease when thin-film RLC models are used in place of the ideal components, and 5% decrease when ceramic RLC are used in place of the thin-film components. On the other hand, less than 5% of degradation to efficiency is caused by realistic FR4 material properties.

Figure 3.27 is a photograph of the fabricated enhanced voltage doubler PCB design shown in Figure 3.24. High quality components are used, and their parameter values are initially adapted from the mixed simulation in Figure 3.25. The value of the load resistor

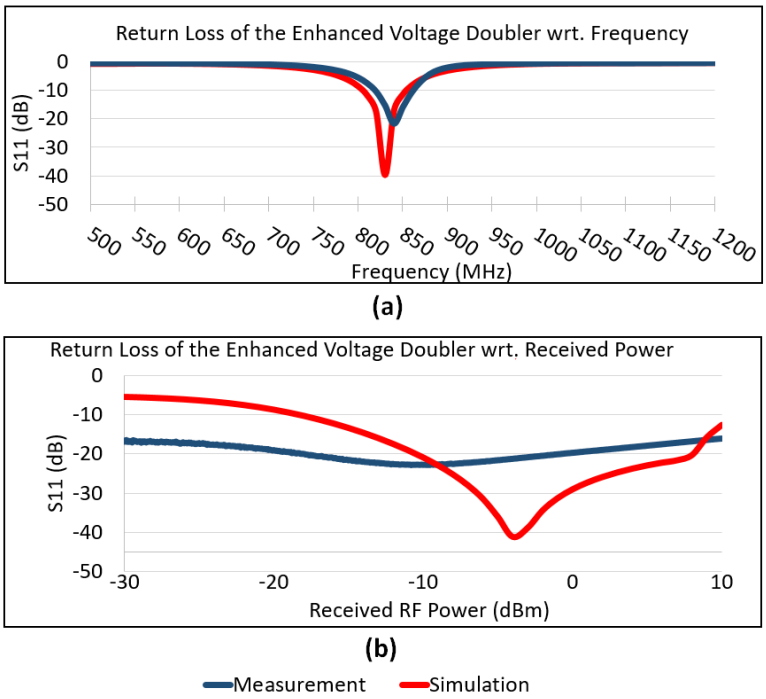

Figure 3.28: Comparison of measured and simulated return loss of the enhanced voltage doubler with respect to (a) frequency, and (b) received RF power.

and the matching network are fine-tuned by trial-and-error until an acceptable return loss is reached.

The fabricated rectifier prototype is measured on a VNA (Agilent PNA N5222a), and the 1-port S-parameter results are compared against the mixed simulation results as shown in Figure 3.28. Under a frequency sweep, the measured and simulated return loss are closely matched; the measured bandwidth is approximately 30-MHz at -15dB. When the input power is swept, the results have some visual similarities in that the measured result could simply be shifted to accommodate a lower power. Regardless, the measured return loss is acceptable to achieve high RF-to-DC conversion efficiency.

Figure 3.29 is an evaluation of the enhanced voltage doubler prototype when its input terminal is connected to a signal generator that is outputting a continuous wave at 837-MHz. An oscilloscope with a high impedance probe is used to measure the voltage at the resistive load of the rectifier. Figure 3.29a shows agreement between the measured and simulated DC voltage up until approximately 5dBm. The discrepancy in output voltage stems from an inconsistent description in the diode's SPICE model. At 2dBm received RF

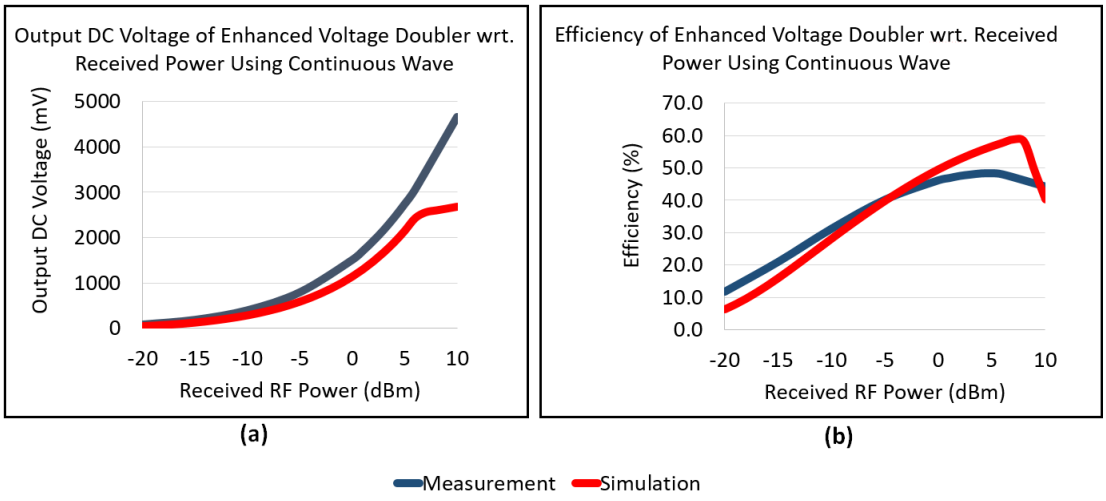

Figure 3.29: Comparison of measured and simulated (a) output DC voltage, and (b) RF-to-DC conversion efficiency of the enhanced voltage doubler.

power, the rectifier prototype is able to produce 2V DC. With a known load resistance (R_{Load}=4916ohms), Figure 3.29b depicts the measured RF-to-DC conversion efficiency as calculated based on the definition given in Equation 3.1. The measured efficiency closely matches that of the simulated up to 0dBm. The discrepancy is likely also diode driven, due to a more significant change in input impedance of the diode at higher power levels. At 2dBm received RF power, the efficiency is 47%. The peak efficiency is 49% at 5dBm of received RF power.

3.4 Integration and Measurement of the Rectenna Prototype

With a rectifier capable of converting 2dBm RF power into nearly 0dBm of DC power at 2V, it is assembled with the GSM-850 lens-dipole, the model-eye, and the matching circuit for matching the antenna to the rectifier. The entire rectenna assembly is connected together via female-female SMA adapters as shown in Figure 3.30.

A cellular emulation setup is put together to evaluate the rectenna as shown in Figure 3.31a. A Rohde and Schwarz CMU is used to emulate a cellular base-station. The green horn antenna is connected to the CMU's output/input RF port, and the RF power level is

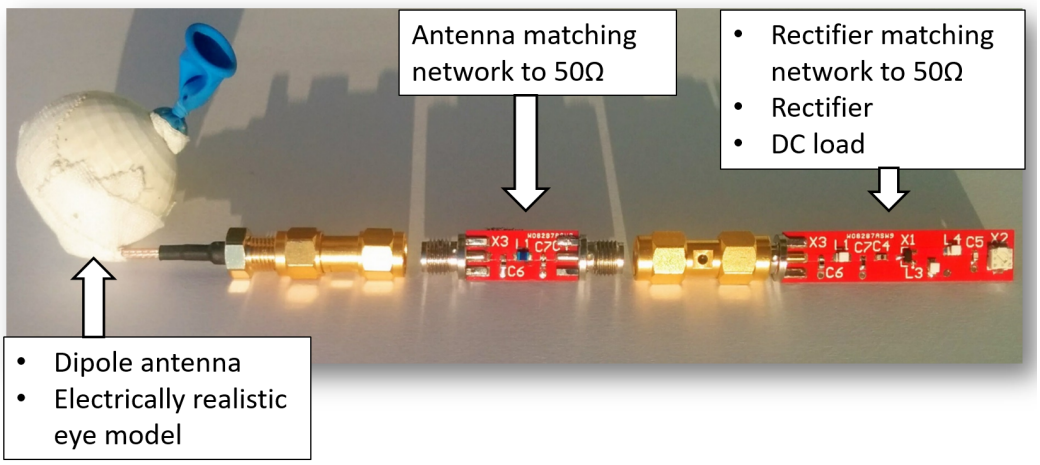

Figure 3.30: Integration rectenna with the enhanced voltage doubler as rectifier and GSM-850 lens-dipole as antenna.

significantly attenuated to ensure that a mobile device would treat the CMU as a faraway base-station. A smartphone is placed at a distance close enough from the CMU to maintain a steady voice call, but the attenuation at the CMU RF port makes the smartphone transmit at the highest power level (TRP=33dBm). The CMU is configured to communicate with the smartphone on the GSM-850 channel. The rectenna is place approximately 18cm from the smartphone, which is a distance that a person can still comfortably operate a smartphone. The output voltage at the load is measured on the oscilloscope, and the reading is shown in Figure 3.31b. The oscilloscope shows that the rectenna is able to generate a peak output DC voltage of 2.1V, which is equivalent of 1mW DC by considering the R_{Load}. The periodic square waves are due to the communication behavior of the GSM-850 network, where the smartphone only transmits in short burst. The time interval of each burst is 0.58ms, which is long enough to accommodate many cycles of the complete data transmission for radio transmitters with a data rate in the Mbps range.

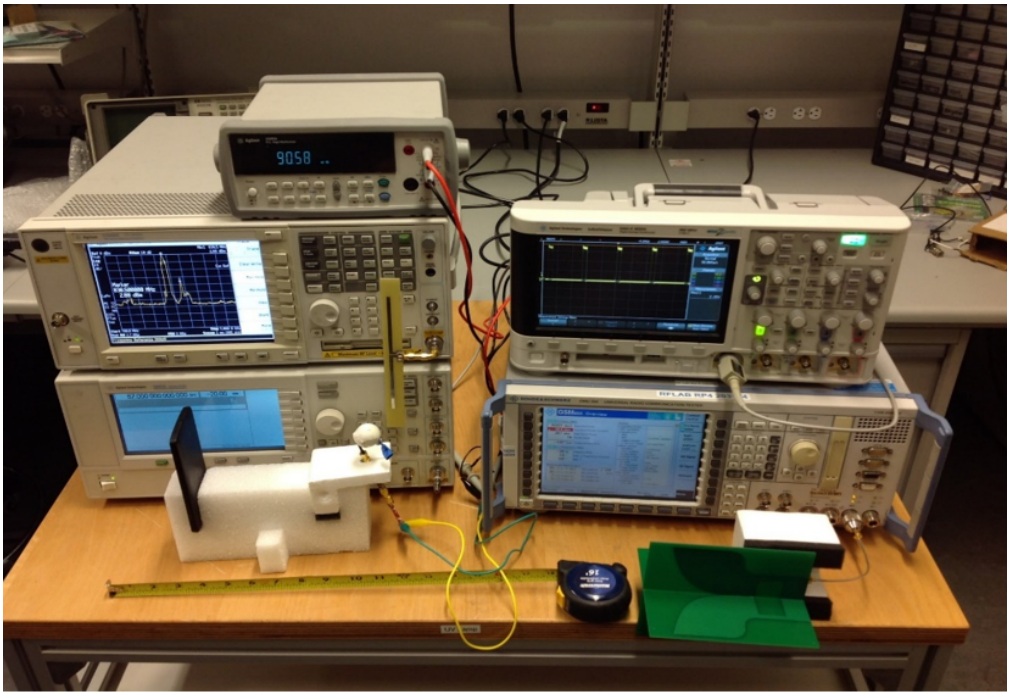

(a)

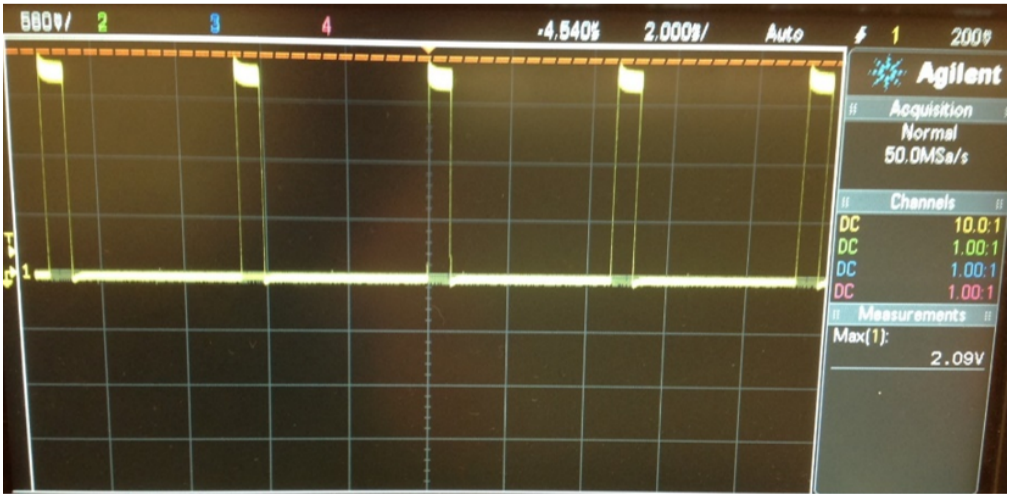

(b)

Figure 3.31: (a) Measurement setup of the rectenna in its intended use-case scenario, and (b) the measured output DC voltage.

Chapter 4

Backscattering Telemetry from Smart Contact Lens to Smartphone

The smart contact lens is able to be powered by a smartphone from 18cm away as shown by measurement in Chapter 3. This Chapter aims to construct a proof-of-concept prototype for determining the feasibility of backscattering from the smart contact lens over the 18cm distance via Bluetooth Low Energy.

4.1 System Implementation of the Backscatter Proof of Concept

The proof of concept prototype will focus on the development of the backscatter module that would be implemented on the smart contact lens. Based on the principles of system operation explained in Chapter 2, the major components involved in this prototype are shown in Figure 4.1: a signal generator is used for transmitting the continuous single-tone carrier at 2412-MHz to mimic the proposed usage of Wi-Fi Channel-1 on a smartphone as the RF source; a Bluetooth tester is tuned to a center frequency of 2416-MHz for demodulating any BLE signal on Bluetooth Channel-38; the backscatter module for the smart contact lens is constructed from a FPGA, a discrete RF FET, and an antenna assembly.

The energy consuming tasks of the backscatter module include generating a baseband in the form of a BLE frame as discussed in Chapter 2.1, up-shifting the baseband to an intermediate frequency via a sub-carrier as discussed in Chapter 2.2.2, and creating the

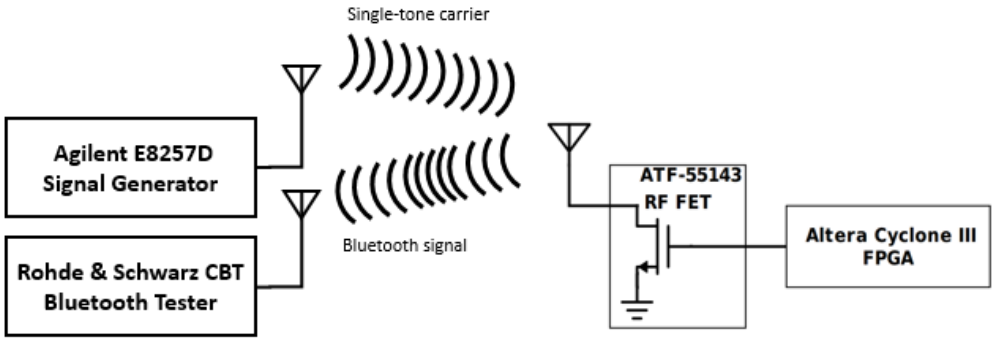

Figure 4.1: System block diagram of the backscatter module.

BFSK constellation by driving the RF-FET. The backscatter module operates independently from the arrival of the single-tone carrier, because the microelectronic components on the smart contact lens will remain in continuous operation powered by the rectified GSM-850 emissions. This mode of backscatter communication is reflected by the proof of concept implementation of digital circuits on the FPGA as shown in Figure 4.2 and Figure 4.3.

4.1.1 Implementation of Digital Hardware in FPGA

The backscatter module has three states of operation implemented as a state-machine on the FPGA depicted in Figure 4.2. The device enters a "Starting" state when powered on, which describes a brief period for components to initialize. As soon as the component initialization is ready, a BLE frame is constructed in the "Streaming" state, and the content of the frame is bit-wise shifted from the most significant bit to the least significant bit. The backscatter module goes into an "Idle" state until the next Streaming cycle. The minimum duration of idling is dependent on technology specification of the BLE protocol. The maximum idling duration is a tradeoff between the probability of signal detection by the receiver, and the power consumption rate of the backscatter module on the smart contact lens. The idling interval used in this proof of concept prototype is made to be same as an iBeacon-enabled Apple iPad4 at 31ms.

The core components of the backscatter module in the FPGA is described in Figure 4.3. The state-machine is driven by a crystal oscillator referenced at a clock frequency of 50-MHz. The reference clock is further divided into two specialized clocks for the intent of bit-wise shifting the BLE baseband, and up-shifting the baseband to a intermediate frequency used by the sub-carrier. The Altera PLL IP Core (ALTPLL) is used for the

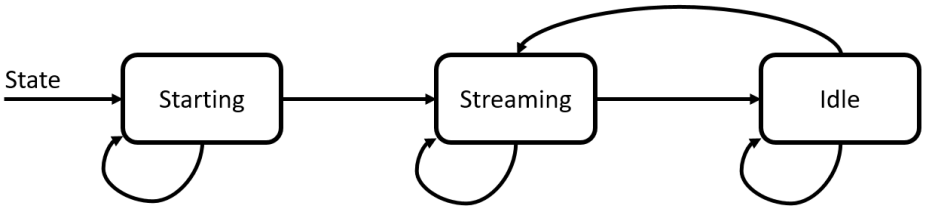

Figure 4.2: A state-machine for controlling BLE logic on the FPGA.

frequency multiplication of the clocks: a $\frac{1}{50}$ multiplication from the 50-MHz reference clock generates a 1-MHz clock to match the specified BLE data rate, and a $\frac{31}{4}$ multiplication from the 50-MHz reference clock generates a 387.5-MHz clock to establish the sub-carrier.

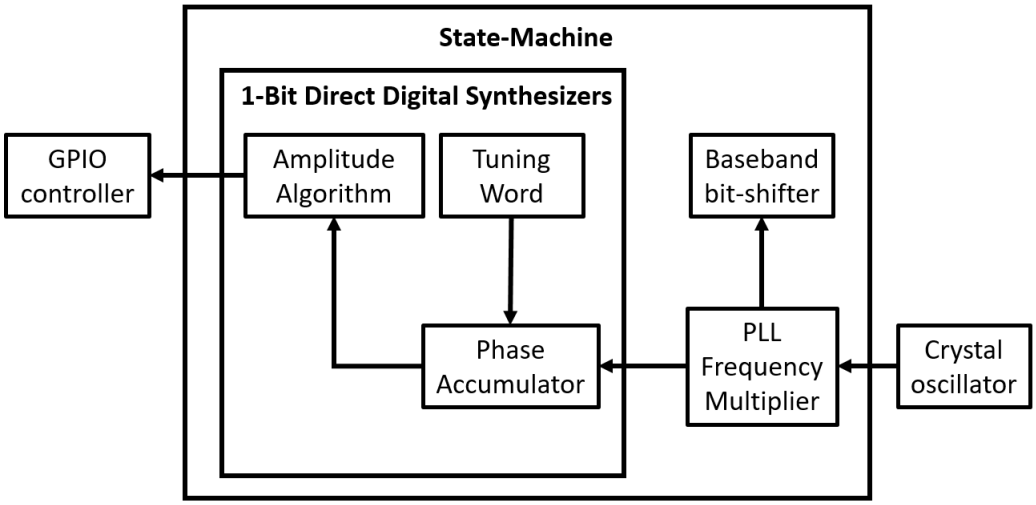

Figure 4.3: A block diagram of the digital circuit for generating a BLE signal at the intermediate frequency.

The 1-MHz data rate of the basic BLE protocol is generated by bit-wise shifting the digital baseband on the backscatter module in sync to the 1-MHz clock. Meanwhile, a 1-bit Direct Digital Synthesizer (DDS) up-shifts the 1-MHz baseband to an intermediate frequency centered at 14-MHz with a frequency deviation that must be greater than 185-KHz as mentioned in Chapter 2.1. The frequency deviation is achieved by the DDS tracking the phase information of the sub-carrier signal based on the 387.5-MHz clock. This phase information is artificially generated by the "Phase Accumulator", which is a modulo counter over a single period of the sub-carrier. Equation 4.1 shows the frequency accuracy that

can be controlled by manipulating several parameters that affect the incremental value of phase that is accumulated.

$$f_{center} \pm f_{deviate} = \frac{\Delta\theta_{center} \times f_{clock}}{2^N} \pm \frac{\Delta\theta_{deviate} \times f_{clock}}{2^N} \tag{4.1}$$

This proof of concept prototype has used an intermediate frequency of 14-MHz with ±265-KHz by substituting the following values in Equation 4.1:

- $\Delta\theta_{center}$: 296°
- $\Delta\theta_{deviate}$: 5°
- N (Length of the phase accumulator, in bits): 13
- f_{clock}: 387.5-MHz

The total length of the phase accumulator is carefully chosen to be 2^{13}. It is the largest integer that produces the fine $\Delta\theta_{deviate}$ in the KHz range. Due to the limitation in parametric freedom, the f_{clock} is made to be 387.5-MHz to ensure that the center frequency is at 14-MHz.

The phase information also plays a part in determining the amplitude of the sub-carrier signal. Traditionally, the digital amplitude information that corresponds to the phase of a complete cycle of a waveform (i.e. a sinusoidal sub-carrier) is stored in non-volatile memory as a lookup table. The DDS cyclically steps through the lookup table and feeds the amplitude information to a DAC for generating the desired analog waveform [51]. In this prototype, the sub-carrier is constructed in a square wave format, which means that the DDS only has to expend 1 bit for flipping the sub-carrier signal between low and high amplitude, which makes the DAC obsolete in this implementation. The duty cycle of a sub-carrier period is kept at 50% by assigning the center of the total phase accumulator length as the position to flip the amplitude.

RTL simulation is conducted on the state machine in ModelSim. Figure 4.4a shows the sub-carrier and the baseband. It is difficult to visually observe the minute differences in $\Delta\theta_{deviate}$ between the baseband bit 0 and bit 1, but the periods of the sub-carrier are slightly longer during a baseband bit 0. Figure 4.4b shows that the amplitude of the sub-carrier flips from a bit 0 to a bit 1 at approximately the phase number of 4671°, which is close to half of the total phase accumulator length. The phase position of the sub-carrier amplitude flip is not necessarily consistent for every period, because the resolution of the

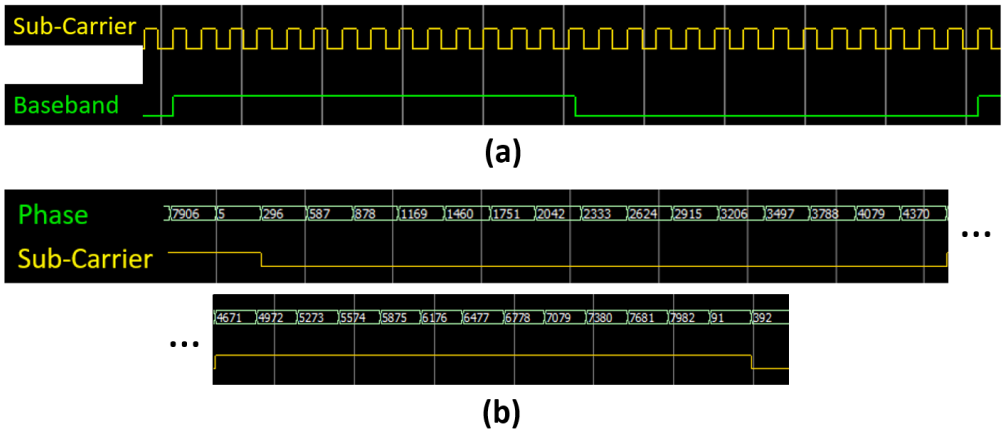

Figure 4.4: Waveform of the FPGA prototype generated in a RTL simulation: a) FM sub-carriers in relation to baseband; b) $\Delta\theta$ of a sub-carrier period.

phase increment is limited by the clock frequency. The waveform is always continuous, because the initial phase of each period of the waveform is carried over from the previous period, due to the behavior of the modulo phase counter.

4.1.2 Modulation and Demodulation of the Baseband

A mathematical model of a frequency-shifting digital backscatter system is written in MATLAB to demonstrate the procedures involved in the frequency synthesis, modulation, filter, and demodulation of digital data. Since this MATLAB model does not involve characterization of communication error, the operating frequencies of the model is reduced to the hundred-KHz range to minimize sampling size, which shortens calculation time of the model.

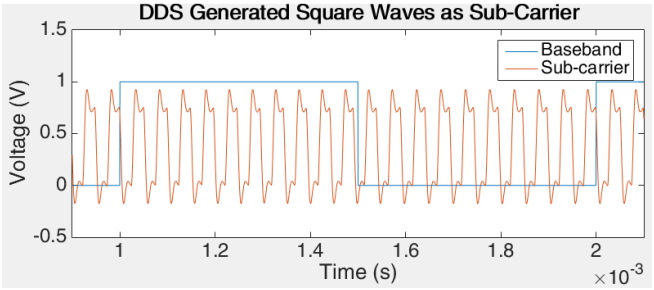

Figure 4.5: A baseband modulated non-ideal unipolar square wave as sub-carrier.

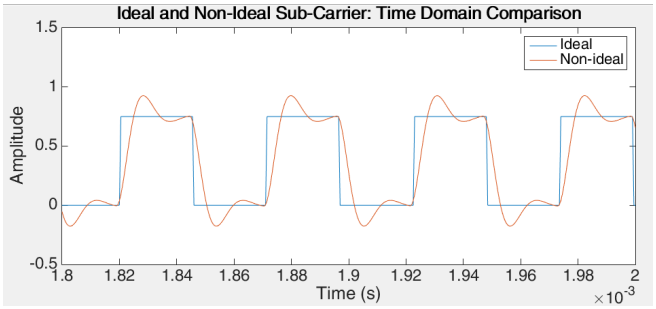

Figure 4.6: Comparison of the ideal and non-ideal sub-carrier waveform in the time domain.

Figure 4.5 shows the baseband and the sub-carrier that would be generated by the backscatter module. The MATLAB simulated sub-carrier is generated using the same 1-bit DDS technique as described in Figure 4.3. The sub-carrier is considered as a non-ideal waveform to include the effect of parasitics capacitance and inductance that could exhibit in the fabricated PCB prototype. Comparing to an ideal square wave, the non-ideal sub-carrier in Figure 4.6 has a finite rise and fall time, as well as a slight overshoot.

The frequency domain in Figure 4.7 shows that the fundamental component of the non-ideal sub-carrier is identical to the ideal waveform, and the main differences are in the higher order harmonics. It is also observed that the fundamental component of the sub-carrier is frequency modulated in a narrow band.

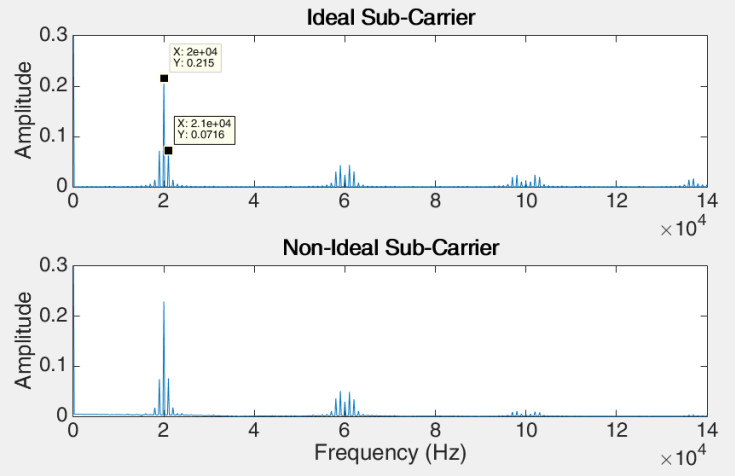

Figure 4.7: Comparison of the ideal and non-ideal sub-carrier waveform in the frequency domain.

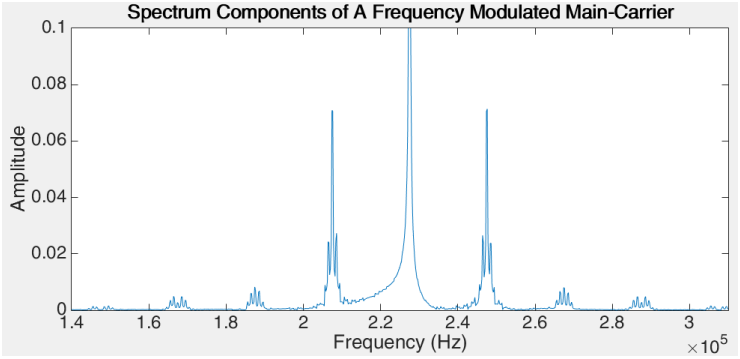

Figure 4.8: Frequency spectrum components of a frequency modulated main-carrier.

Figure 4.8 shows a main-carrier modulated in frequency by the sub-carrier, which represents the backscattered signal from the backscatter module. The original baseband data is up-shifted as sidebands of the main-carrier, which can be extracted from the fundamental component, or any of the higher order harmonics. The baseband data is best preserved in the fundamental component due to its much higher amplitude.

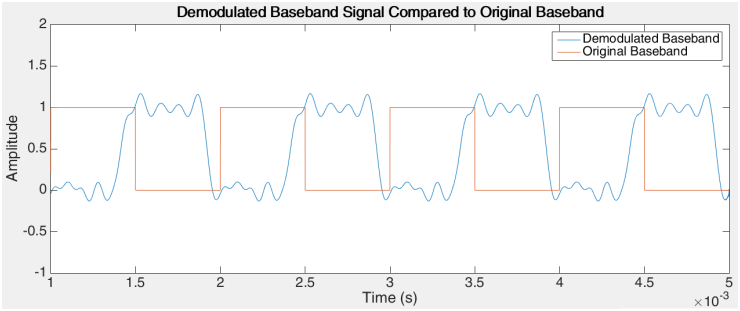

Figure 4.9: Comparison of demodulated baseband and original baseband in time domain.

The demodulation of the backscattered signal follows three steps: first, bandpass filter the fundamental component; second, down-shift the fundamental component to baseband; finally, low-pass filter the demodulated baseband to smoothen the signal. Figure 4.9 shows that the demodulated signal is shifted in time domain. This is due to a delay in phase.

4.2 Impedance Characteristics of the BS Module

The RF FET is assembled on a PCB with its gate controlled by a binary voltage level outputted from FPGA, and its drain connected to the antenna via a SMA connector. Figure 4.10 shows the complete backscatter module. The interface between the drain of the FET and the antenna defines the BFSK constellation that BLE utilizes for communication.

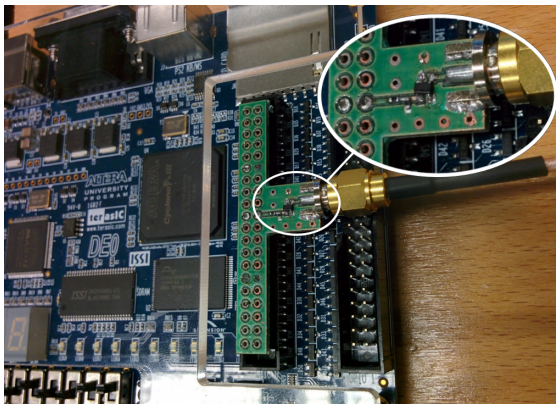

Figure 4.10: The backscatter module prototype.

The RF FET PCB is measured on a VNA (Agilent PNA N5222a) for the drain impedance with referenced to a 50ohms port. The drain impedance in two conditions are measured by applying a constant voltage at the gate to create an open-circuit and short-circuit connection from the drain to ground via the source terminal.

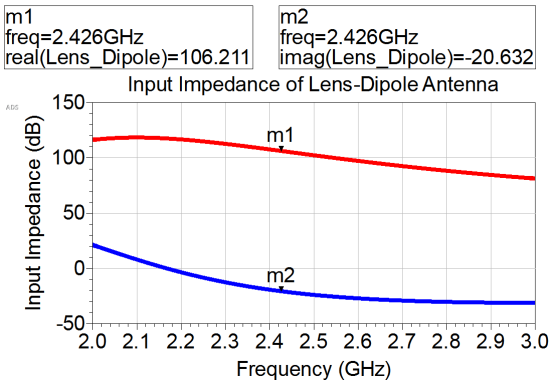

Figure 4.11: Real and imaginary part of the GSM-850 lens-dipole impedance at 2426-MHz.

The backscatter module uses an unmatched antenna assembly similar to the GSM-850 lens-dipole antenna discussed in Chapter 3.2; its input impedance at 2426-MHz is shown in Figure 4.11. The use of an unmatched antenna is due to the fact that ideal matching condition should be prioritized to the GSM-850 Uplink band for energy harvesting purposes.

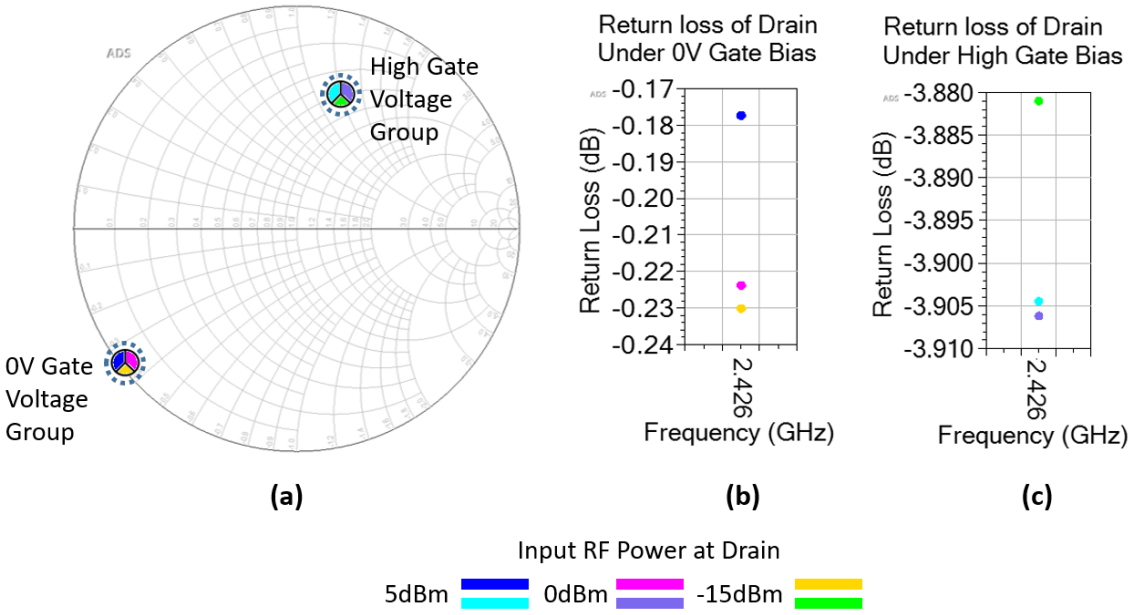

Figure 4.12: Reflection coefficient and return loss of the load modulator at different input power level: a)reflection coefficient ; b) return loss under 0V gate bias; c) return loss under high voltage gate bias.

The reflection coefficient at the drain with reference to the antenna can be found by replacing the 50ohms port impedance with the antennas input impedance at 2426-MHz. This is shown in Figure 4.12. S-Parameter measurements are conducted for six separate bias conditions on the RF FET: when the gate is biased at 0V, three RF power levels are considered at the drain; the same three RF power levels are considered at the drain, when the gate is biased high. It is observed in Figure 4.12a that the gate voltage has separated the reflection coefficient into two distinct group between 0V and high voltage with minimal impact from the different power level at the drain. Figure 4.12b and Figure 4.12c show that the return loss at the drain is approximately 3dB greater under high voltage gate bias; this imbalance does not pose any significant negative effect to impede the validity of the backscatter module prototype.

4.3 Frequency Characteristics of the BS Module

The backscatter module and prototype test-bed described in Figure 4.1 are implemented here to validate the theory of operation from the perspective of the BLE modulation performance.

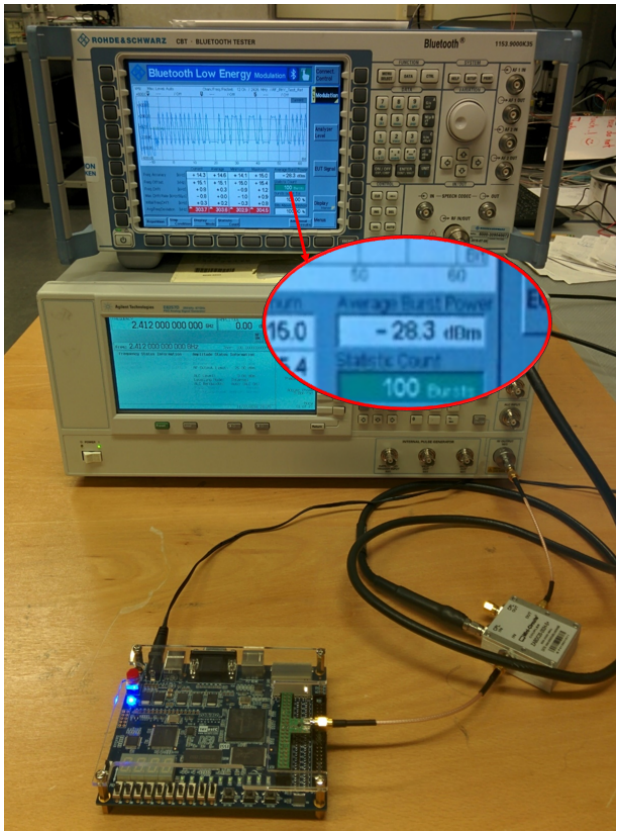

Figure 4.13: The backscattering module prototype interfaced with the test equipment via coaxial cables.

Figure 4.13 shows that the measurement setup utilizes an Agilent E8257D signal generator as the RF source in place of Wi-Fi source from a smartphone, and a Rohde & Schwarz CBT as the BLE receiver in place of smartphone Bluetooth receiver. However, a Mini-Circuit bi-directional coupler (ZABDC20-252H) and common 50ohms coaxial cables are used in place of antennas as the transmission channel to establish a predictable test environment. The coupler's mainline terminals are its input and output ports, which are connected to the FET modulator and the signal generator, respectively. The coupled

forward port is connected to the CBT, while the coupled reverse port is terminated by a 50ohms load. This configuration allows the power from the signal generator to reach the FET modulator with negligible loss, and also to couple the backscattered signal from the FET modulator to the CBT for detection at a predictable input power.

4.3.1 A Study of Effects from the Coupler

The signal generator is configured to generate a single-tone carrier of 0dBm at the generator's output port. It can be observed in Figure 4.13 that the average received power from a burst of binary data in the BLE frame, at the RF port of the Bluetooth Tester, is -28dBm. Figure 4.14 shows an ADS circuit simulation of the measurement set-up, which is used to determine the origin of losses that resulted in the -28dBm received power.

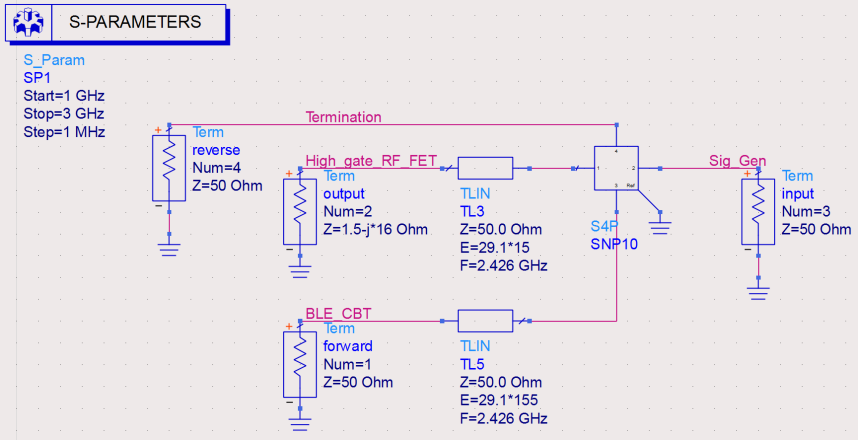

Figure 4.14: ADS schematic simulation of the coupler-connected measurement setup.

A data block is used to represent the S-parameter of the bi-directional coupler by using the provided data file from the Manufacturer. 50ohms terminals are used to represent the port of the measurement equipment, while the backscatter module is treated as a linear component with a constant load impedance at the intended frequency (i.e. 2426-MHz). The values of the load impedance (for both 0V gate bias and high voltage gate bias) are determined from the measured drain impedance of the RF FET PCB with reference to a 50ohms port impedance. Ideal transmission lines are measured precisely in length to replicate the coaxial cables' effect on the signal phase.

Figure 4.15 shows the insertion loss between the backscatter module to the Bluetooth tester in the ADS simulation. The insertion loss between the signal generator and the

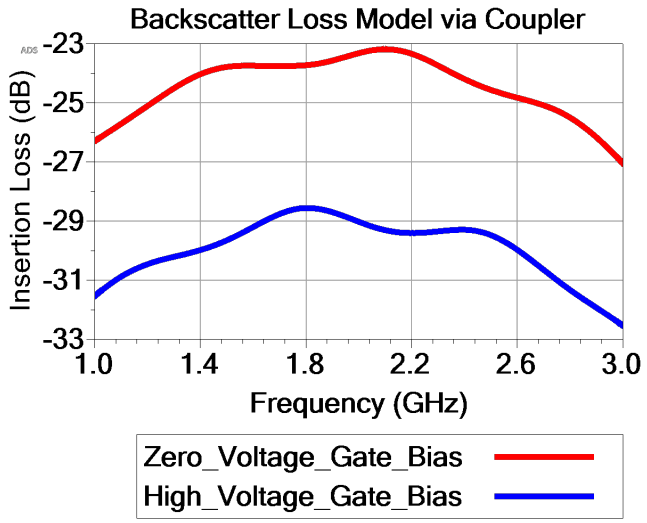

Figure 4.15: Losses due to coupler in The Backscattered Signal.

backscatter module is not considered, because it is known that the mainline loss between a bi-directional coupler's input and output port is negligibly small when compared to the losses from coupling. It can be observed that the average insertion loss caused by the two state of gate bias is approximately 27dB, which is in agreement with the measurement in Figure 4.13.

4.4 Modulation Performance of the BS Module in Measurement

The Rohde & Schwarz CBT is an all-around Bluetooth tester. In BLE mode, it has the capability to listen to incoming BLE signals, and to trigger at the rising edge of the burst's zeroth bit. Then, it would be able to perform analysis on the power, modulation, and spectrum behavior of the FET modulator, provided that the received signal has a correct BLE frame on the bit level. The demodulator in the CBT could be configured to the identical specification as the Bluetooth receiver on a smartphone.

Figure 4.16 shows the first 48 bits of a BLE burst, which are defined by the BLE advertisement frame structure—they are the Preamble and Access Address of a frame. Due to the short time scale, several pictures of the screen are taken at sequential time points of the burst; these pictures are stitched together to display a continuous bit stream. Visually,

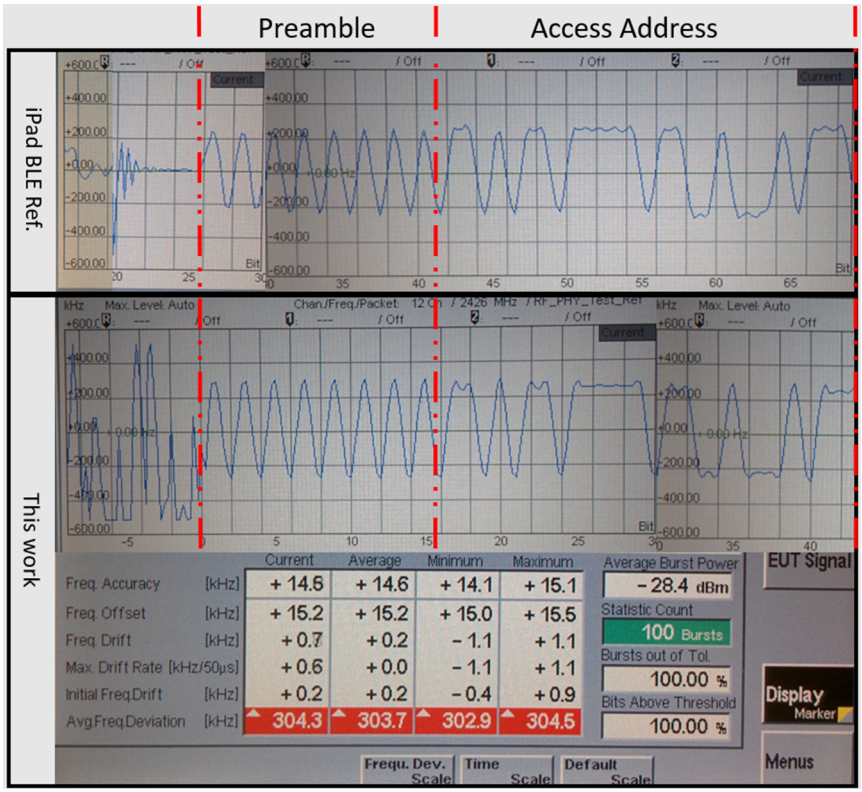

Figure 4.16: CBT results of a demodulated BLE frame compared between different sources.

there is an excellent match when comparison is made between the demodulated signal emitted from an iPads iBeacon emulator with that of the backscattered signal from the backscatter module. The numerical summary of the frequency behavior also indicates a modulator that is within the specifications of commercial BLE devices. The frequency deviation highlighted in red indicates a value above ideal frequency modulation index of 0.45 to 0.55, but this does not impact the smartphones ability to demodulate the backscattered signal. The Bluetooth tester also provides an evaluation of the modulation characteristics (frequency accuracy, offset, drift etc.) of the backscatter module from analyzing 100 consecutive backscattered bursts of the same BLE frame. The exact acceptable range of error is configured from the Bluetooth Core Specification.

4.5 Backscattered BLE Power from A Smart Contact Lens Antenna

A measurement setup to test the backscatter module wirelessly with antennas is shown in Figure 4.17. The equipment used here is exactly as described by the block diagram of the system in Figure 4.1. The transmitting dipole antenna and the receiving dipole antenna for the signal generator and the Bluetooth tester respectively are handmade from copper tape. The transmitter and receiver dipole antennas are fixed in place in free-space with a 10cm gap between them to minimize mutual coupling. The backscatter module utilizes the GSM-850 lens-dipole as the scattering antenna along with the model-eye to include the expected losses from the eye tissue. The entire backscatter module is aligned and placed 23cm from the transmitter and receiver dipole antennas. This distance is farther than the distance used in energy harvesting as demonstrated in Figure 3.31 of Chapter 3. The signal generator is configured to output a 20dBm 2412-MHz single-tone carrier at its RF port. Additional 40dB attenuation is added to the RF port of the Bluetooth tester, due to the close by high power RF source from the signal generator.

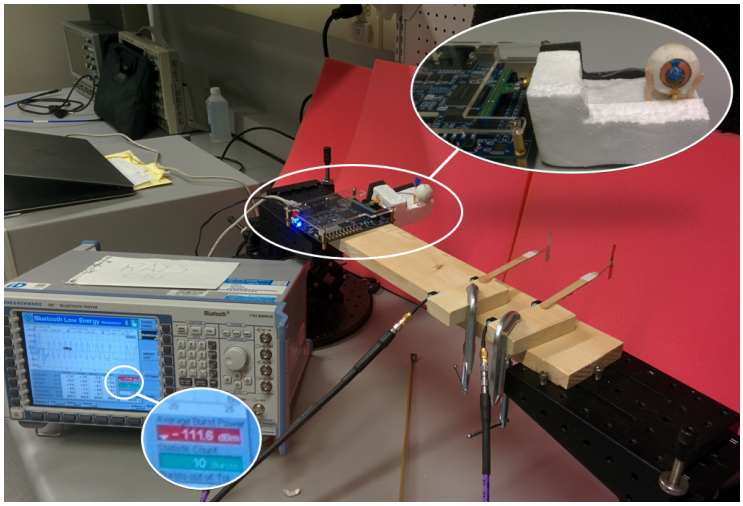

Figure 4.17: Measurement setup for evaluating the wireless backscatter module.

The average burst power of the received signal by the Bluetooth tester from the backscatter module is -111.6dBm, which is highlighted in red as a warning that it is approaching the minimum threshold in receiver sensitivity. The received power is equivalent to a total of 91.6dB loss in the wireless channel by considering the transmitting power and the added attenuation.

Chapter 5

Conclusion and Future Work

This thesis proposed an all-in-one solution on using a smartphone to wirelessly power a smart contact lens, and also collect glucose data directly from it. A dipole antenna is proposed, designed, and tested for capturing smartphone radio emission on the smart contact lens. The eye's effect of the antenna is characterized by changes in return loss. The design procedure and usage of a low-cost electrically realistic model-eye is presented as a measurement platform for on-lens antenna design validation. A well-tuned rectifier PCB is fabricated and measured with results closely match to those from simulation. It is found in measurement that the energy harvester can capture 1mW at 2.1V DC for the smart contact lens from a smartphone placed 18cm away, which sufficiently satisfies the power budget for many low power microelectronic circuits used for glucose detection and wireless data transmission. Compared to matured eye-mounted systems in related works, the use of a smartphone as source is proven to be viable, if the energy harvesting rectenna is implemented as described in this proof of concept design. A backscatter module is developed as an assembly of digital logic on FPGA and an analog frontend on PCB, demonstrating in measurement that the smart contact lens is capable of transmitting glucose data directly to a smartphone over a 23cm distance.

Regarding the energy harvester, the next step is to implement the rectifier structure on an IC platform, and evaluate the rectenna as a part of a real contact lens when worn. Regarding the backscatter module, the next step is to use a smartphone in place of the signal generator, and demodulate the backscattered Bluetooth Low Energy signal directly on the smartphone instead of the Bluetooth tester.

References

[1] Centers for Disease Control and Prevention, "National diabetes statistics report: Estimates of diabetes and its burden in the united states," Department of Health and Human Services, Atlanta, GA: U.S., Tech. Rep., 2014.

[2] Canadian Diabetes Association, "Diabetes statistics in canada," Available at http://www.diabetes.ca/how-you-can-help/advocate/why-federal-leadership-is-essential/diabetes-statistics-in-canada#_ftn1 (2017/01/12).

[3] World Health Organization, "Diabetes fact sheet," Available at http://www.who.int/mediacentre/factsheets/fs312/en/index.html (2017/01/12).

[4] Canadian Diabetes Association, "Self-monitoring of blood glucose," Available at http://www.diabetes.ca/clinical-practice-education/professional-resources/self-monitoring-of-blood-glucose (2017/01/12).

[5] U.S. Food and Drug Administration, "Premarket approval: Dexcom g4 platinum contiuous glucose monitoring system," Available at http://www.accessdata.fda.gov/scripts/cdrh/cfdocs/cfpma/pma.cfm?id=P120005 (2017/01/12).

[6] S. Vaddiraju, D. J. Burgess, I. Tomazos, F. C. Jain, and F. Papadimitrakopoulos, "Technologies for continuous glucose monitoring: Current problems and future promises," *Journal of Diabetes Science and Technology*, vol. 4, no. 6, pp. 1540–1562, November 2010.

[7] E. Renard, "Implantable continuous glucose sensors," *Current Diabetes Reviews*, vol. 4, no. 3, pp. 169–174, August 2008.

[8] G. Rao, P. Glikfeld, and R. Guy, "Reverse iontophoresis: Development of a noninvasive approach for glucose monitoring," *Pharmaceutical Research*, vol. 10, no. 12, pp. 1751–1755, December 1993.

[9] S. Gebhart, M. Faupel, R. Fowler, C. Kapsner, D. Lincoln, V. McGee, J. Pasqua, L. Steed, M. Wangsness, F. Xu, and M. Vanstory, "Glucose sensing in transdermal body fluid collected under continuous vacuum pressure via micropores in the stratum corneum," *Diabetes Technology and Therapeutics*, vol. 5, no. 2, pp. 159–166, July 2004.

[10] J. Pandey, Y.-T. Liao, A. Lingley, R. Mirjalili, B. Parviz, and B. Otis, "A fully integrated rf-powered contact lens with a single element display," *IEEE Transactions on Biomedical Circuits and Systems*, vol. 4, no. 6, pp. 454–461, December 2010.

[11] W. Gao, S. Emaminejad, H. Y. Y. Nyein, S. Challa, K. Chen, A. Peck, H. M. Fahad, H. Ota, H. Shiraki, D. Kiriya, D.-H. Lien, G. A. Brooks, R. W. Davis, and A. Javey, "Fully integrated wearable sensor arrays for multiplexed in-situ perspiration analysis," *IEEE Transactions on Biomedical Circuits and Systems*, vol. 529, no. 7585, pp. 509–514, January 2016.

[12] R. D. Munje, S. Muthukumar, and S. Prasad, "Lancet-free and label-free diagnostics of glucose in sweat using zinc oxide based flexible bioelectronics," *Sensors and Actuators B: Chemical*, vol. 238, pp. 482–490, January 2017.

[13] S. B. Lee. (2012) Why do i taste my eye drops? [Online]. Available: https://www.drleesb.wordpress.com/2012/04/12/why-do-i-taste-my-eye-drops/

[14] N. Farandos, A. Yetisen, M. Monteiro, C. Lowe, and S. H. Yun, "Contact lens sensors in ocular diagnostics," *Advanced Healthcare Materials*, vol. 4, no. 6, pp. 792–810, November 2014.

[15] J. Lane, D. Krumholz, R. Sack, and C. Morris, "Tear glucose dynamics in diabetes mellitus," *Current Eye Research*, vol. 31, no. 11, pp. 895–901, March 2006.

[16] R. Doelling, "Potentiostats," Available at https://www.bank-ic.de/encms/downloads/potstae2.pdf (2017/01/12), 2000.

[17] J. de Juan Sanz. (2015) Contact lenses to monitor glucose levels: A sweet solution for diabetic patients? [Online]. Available: www.mappingignorance.org/2015/01/02/contact-lenses-monitor-glucose-levels-sweet-solution-diabetic-patients/

[18] B. Otis, D. Yeager, and A. Nelson, "Methods and systems for identification of an eye-mountable device," Patent US 20 150 002 270, January 1, 2015. [Online]. Available: https://www.google.com/patents/US20150002270

[19] Z. Liu, "Contact lenses having two-electrode electrochemical sensors," Patent US 20 140 194 713, July 10, 2014. [Online]. Available: https://www.google.ch/patents/US20140194713

[20] N. Pletcher and B. Otis, "Contact lenses with hybrid power sources," Patent US 20 140 192 311, July 10, 2014. [Online]. Available: https://www.google.com/patents/US20140192311

[21] K. Raizada and M. Sridhar, "Nomogram for spherical rgp contact lens fitting in patients with pellucid marginal corneal degeneration (pmcd)," *Eye and Contact Lens*, pp. 769–772, January 2012.

[22] C. Maldonado-Codina, and N. Efron, "Impact of manufacturing technology and material composition on the surface characteristics of hydrogel contact lenses," *Clinical and Experimental Optometry: Journal of the Australian Optometrical Association*, vol. 88, pp. 396–404, 2005.

[23] Y. T. Liao, H. Yao, A. Lingley, B. Parviz, and B. P. Otis, "A 3uw cmos glucose sensor for wireless contact-lens tear glucose monitoring," *IEEE Journal of Solid-State Circuits*, vol. 47, no. 1, pp. 335–344, January 2012.

[24] J. F. Ensworth, and M. S. Reynolds, "Every smart phone is a backscatter reader: Modulated backscatter compatibility with bluetooth 4.0 low energy (ble) devices," *2015 IEEE International Conference on RFID*, pp. 78–85, April 2015.

[25] J. Abraham. (2014) Understanding bluetooth advertising packets. [Online]. Available: http://j2abro.blogspot.ca/2014/06/understanding-bluetooth-advertising.html

[26] S. J. Thomas, "Modulated backscatter for low-power high-bandwidth communication," PhD dissertation, Duke University, 2013.

[27] H. Yao, C. Marcheselli, A. Afanasiev, I. Lhdesmki, and B. A. Parviz, "A soft hydrogel contact lens with an encapsulated sensor for tear glucose monitoring," *2012 IEEE 25th International Conference on Micro Electro Mechanical Systems (MEMS)*, pp. 78–85, April 2015.

[28] Z. Xiao, X. Tan, X. Chen, S. Chen, Z. Zhang, H. Zhang, J. Wang, Y. Huang, P. Zhang, L. Zheng, and H. Min, "An implantable rfid sensor tag toward continuous glucose monitoring," *IEEE Journal of Biomedical and Health Informatics*, vol. 19, no. 3, pp. 910–919, May 2015.

[29] N. Sangary, Y. Qi and G. Shaker, "Multiband handheld antenna design and test techniques: Recent advances and challeneges," *Short Course, 2010 IEEE International Symposium on Antennas and Propagation*, 2010.

[30] (1999) 3gpp ts 05.05 version 8.20.0. [Online]. Available: https://portal.3gpp.org/desktopmodules/Specifications/SpecificationDetails.aspx?specificationId=258

[31] D. Liebl, and B. Schulz. (2015) 1ma255: Lte and bluetooth in- device coexistence with wlan. [Online]. Available: https://www.rohde-schwarz.com/us/applications/lte-and-bluetooth-in-device-coexistence-with-wlan-application-note56280-116549.html

[32] X. Tan, S. Chen, Z. Xiao, F. Chen, J. Wang, "A low power potentiostat for implantable glucose sensor tag," *2015 IEEE 11th International Conference on ASIC (ASICON)*, pp. 1–4, November 2015.

[33] S. Ghanabri, and M. Habibi, "Low power potentiostat using switching technique for three electrode amperometric sensors," *2015 23rd Iranian Conference on Electrical Engineering*, pp. 1154–1158, May 2015.

[34] L. Zuo, S. K. Islam, I. Mahbub, and F. Quaiyum, "A low-power 1-v potentiostat for glucose sensors," *IEEE Transactions on Circuits and Systems II: Express Briefs*, vol. 62, no. 2, pp. 204–208, February 2015.

[35] M. M. Ahmadi, and G. A. Jullien, "A wireless-implantable microsystem for continuous blood glucose monitoring," *IEEE Transactions on Biomedical Circuits and Systems*, vol. 3, no. 3, pp. 169–180, June 2009.

[36] M. H. Nazari, M. Mujeeb-U-Rahman, and A. Scherer, "An implantable continuous glucose monitoring microsystem in 180nm cmos," *2014 Symposium on VLSI Circuits Digest of Technical Papers*, pp. 1–4, June 2014.

[37] S. Guan, J. Gu, Z. Shen, J. Wang, Y. Huang, and A. Mason, "Wireless powered implantable bio-sensor tag system-on-chip for continuous glucose monitoring," *2011 IEEE Biomedical Circuits and Systems Conference (BioCAS)*, pp. 193–196, November 2011.

[38] Z. Xiao, X. Tan, X. Chen, S. Chen, Z. Zhang, H. Zhang, J. Wang, Y. Huang, P. Zhang, L. Zheng, and H. Min, "An implantable rfid sensor tag toward continuous glucose monitoring," *IEEE Journal of Biomedical and Health Informatics*, vol. 19, no. 3, pp. 910–919, May 2015.

[39] P. Kamalinejad, K. Keikhosravy, R. Molavi, S. Mirabbasi, and V. C. M. Leung, "An ultra-low-power cmos voltage-controlled ring oscillator for passive rfid tags," *2014 IEEE 12th International New Circuits and Systems Conference (NEWCAS)*, pp. 456–459, June 2014.

[40] F. Song, J. Yin, H. L. Liao, and R. Huang, "Ultra-low-power clock generation circuit for epc standard uhf rdid transponders," *Electronics Letters*, vol. 44, no. 3, pp. 199–201, January 2008.

[41] K. K. Lee and K. Granhaug and N. Andersen, "A study of low-power crystal oscillator design," *2013 NORCHIP*, pp. 1–4, November 2013.

[42] A. Peyman, S. Holden, C. Gabriel, "Dielectric properties of tissues at microwave frequencies," Mobile Telecommunications and Health Research Programme, Chilton, Didcot, Oxfordshire, UK, Tech. Rep., 2005.

[43] C. Gabriel. (2015) Dielectric properties of body tissues. [Online]. Available: http://niremf.ifac.cnr.it/tissprop/htmlclie/htmlclie.php

[44] A. Shameli, A. Safarian, A. Rofougaran, M. Rofougaran, and F. De Flaviis, "Power harvester design for passive uhf rfid tag using a voltage boosting technique," *IEEE Transactions on Microwave Theory and Techniques*, vol. 55, no. 6, pp. 1089–1097, June 2007.

[45] J. P. Curty, N. Joehl, F. Krummenacher, C. Dehollain, and M. J. Declercq, "A model for mu;-power rectifier analysis and design," *IEEE Transactions on Circuits and Systems I: Regular Papers*, vol. 52, no. 12, pp. 2771–2779, December 2005.

[46] G. K. Balachandran, and R. E. Barnett, "A 110 na voltage regulator system with dynamic bandwidth boosting for rfid systems," *IEEE Journal of Solid-State Circuits*, vol. 41, no. 9, pp. 2019–2028, September 2006.

[47] M. Roberg, T. Reveyrand, I. Ramos, E.A. Falkenstein, and Z. Popovi, "High-efficiency harmonically terminated diode and transistor rectifiers," *IEEE Transactions on Microwave Theory and Techniques*, vol. 60, no. 12, pp. 4043–4052, December 2012.

[48] Y. K. Tan, *SUSTAINABLE ENERGY HARVESTING TECHNOLOGIES - PAST, PRESENT AND FUTURE.* Rijeka, Croatia: InTech, 2011.

[49] A. Technologies, "Agilent hsms-285x series surface mount zero bias schottky detector diodes data sheet," http://www.g3ynh.info/circuits/diode_data/Agilent_HSMS-285ser.pdf, 2002.

[50] K. Hosain, A. Z. Kouzani, S. Tye, A. Kaynak, and M. Berk, "Rf rectifiers for em power harvesting in a deep brain stimulating device," *Australasian Physical and Engineering Science in Medicine*, vol. 38, pp. 157–172, March 2015.

[51] E. Murphy, and C. Slattery. (2004) Ask the application engineer33: All about direct digital synthesis. [Online]. Available: http://www.analog.com/en/analog-dialogue/articles/all-about-direct-digital-synthesis.html